Stability of Particle-Mean Flow Interactions in Solid and Hybrid Rockets

A Dissertation Presented for the
Doctor of Philosophy
Degree
The University of Tennessee, Knoxville

Trevor Sterling Elliott
December 2014

"*I started my life with a single absolute: that the world was mine to shape in the image of my highest values and never to be given up to a lesser standard, no matter how long or hard the struggle*."

-Dagny Tagert, *Atlas Shrugged*

To all those that are Family and who share the struggle.

Acknowledgements

First and foremost, I would like to extend my gratitude to my major advisor and committee chair, Dr. Joseph Majdalani, for his continued support of my work and for his drive and determination in the pursuit of excellent work. He has pushed me to achieve work that would not be possible without his guidance.

I would also like to thank my committee members for their review of my work and their invaluable comments and suggestions. Dr. Anusonti-Inthra, Dr. Schulz, and Dr. Parigger all provided many ideas and supportive guidance throughout the progress of this dissertation.

Finally, I would like to thank my family for enduring the long hours, frustrations, complications, and ultimately success of this journey. Without their positive support this work would not be possible.

Abstract

Combustion instabilities associated with rocket motors as a result of unsteady components in the combustion chamber flow have been known to cause pressure oscillations. These pressure oscillations can result in changes to flight characteristics and vibrations translated to the rocket or payload. The unsteady components are comprised of two subcomponents, the vortico-acoustic fluctuations and the hydrodynamic fluctuations. As the vortico-acoustic fluctuations have been investigated in an exhaustive manner this work will focus on the hydrodynamic fluctuations. It has been known that the addition of particles increases specific impulse due to the resulting increase in combustion temperature and mass flow. They also aid in the suppression of fluctuations in the flow field due to added density. However, the drag effects on the gaseous phase slow the gaseous exit velocity reducing the specific impulse.

This work aims to study gaseous flow with particle entrainment within the biglobal framework in an effort to quantify the effects of particles in such flows and what parameters can be varied to optimize stable flow in this configuration. To do so, the linearized Navier-Stokes equations are utilized with the Stokes drag equation for particles. Applying the biglobal ansatz results in a system of equations that can be solved using an eigensolver to yield the entire spectrum of eigenvalues simultaneously. The obtained solutions are compared with previous numerical and experimental results. In summary, the presented work advances the biglobal framework to include particle

entrainment. Furthermore, previous one-dimensional treatments are now extended to include effects along the cross-section of rocket motors.

Table of Contents

List of Figures

Nomenclature

A_{ij} = operator matrix

a = radius of the chamber

B_i = forcing function column vector

B_{ij} = right hand side operator matrix of a matrix pencil

D_N = Chebyshev pseudo-spectral derivative matrix of size N, domain

$\bar{D}_N$ = Chebyshev pseudo-spectral derivative matrix of size N, arbitrary domain

d = weighting coefficients for pseudo-spectral derivative matrices

d_P = particle diameter

I = identity matrix

J = Bessel function of the first kind

L = length of the chamber

l = chamber aspect ratio

M = mean flow component

$\tilde{M}$ = instantaneous flow component

m = general amplitude function

$\breve{m}$ = hydrodynamic unsteady fluctuation

$\hat{m}$ = acoustic unsteady fluctuation

m' = general unsteady fluctuation

$\tilde{m}$ = vortical unsteady fluctuation

m_P	=	mass of one particle
N	=	number of collocation points
n_P	=	number of particles per unit volume
P	=	mean flow pressure
$\tilde{P}$	=	instantaneous flow pressure
p	=	pressure amplitude function
$\breve{p}$	=	hydrodynamic pressure fluctuation
$\hat{p}$	=	acoustic pressure fluctuation
p'	=	general pressure fluctuation
$\tilde{p}$	=	vortical pressure fluctuation
q	=	azimuthal integer wave number
Re	=	Reynolds number
r	=	radial nondimensional coordinate
S	=	Stokes number
T_N	=	Chebyshev polynomial of the first kind
$\boldsymbol{U}$	=	mean flow gas velocity, U_r, U_θ, U_z
$\boldsymbol{U}_P$	=	mean flow particle velocity, $U_{rP}, U_{\theta P}, U_{zP}$
U_N	=	Chebyshev polynomial of the second kind
$\tilde{U}$	=	instantaneous flow velocity

u	=	velocity amplitude function
$\breve{u}$	=	hydrodynamic velocity fluctuation
$\hat{u}$	=	acoustic velocity fluctuation
u'	=	general unsteady velocity fluctuation
$\tilde{u}$	=	vortical velocity fluctuation
u_h	=	headwall injection constant
X_P	=	particle mass concentration
z	=	axial nondimensional coordinate

Subscripts

G	=	denotes gas
N	=	denotes Chebyshev polynomial order
P	=	denotes particle
h	=	denotes headwall property
i	=	denotes a matrix row or vector element
ii	=	denotes a diagonal matrix or diagonal element
ij	=	denotes a matrix
j	=	denotes a matrix column
r	=	denotes radial spatial direction
θ	=	denotes tangential spatial direction
w	=	denotes property at the wall

z = denotes axial spatial direction

Symbols

∇ = gradient operator

α = longitudinal wave number

β = ratio of particle to gas mass

ε = $1 / Re$

λ = eigenvalue

μ = dynamic viscosity

ρ_G = gaseous density

ρ_P = particle density

ω = frequency of oscillation, $\omega_r + \omega_i$

ω_r = circular frequency

ω_i = growth rate

ψ = stream function

Chapter 1

Introduction

In the realm of propulsion and power generation, combustion instability has been a long-standing problem. Consequently, this instability has been the focus of studies for many years. While much progress has been made in understanding and designing to avoid combustion instability, there is a need for vast improvements to instability prediction techniques. These improvements can be made as a result of advancements in analytical and computational tools which aid in the capturing of flow characteristics and specification of design parameters. This study furthers works done using the Biglobal analysis technique through the addition of particle entrainment.

1.1 Combustion Instability

Combustion instabilities observed during the combustion process within internal flow devices are not only a product of the combustion process itself but are a result of unsteadiness within the fluid motion. The unsteadiness within internal flow devices primarily results from geometry and fluid interactions. Three typical sources of unsteadiness are protrusions in the flow, a backward facing step, or fluid/wall interactions. These sources result in three types of vortex shedding processes defined as obstacle, angle, and parietal vortex shedding respectively [1]. Flow within a rocket combustion chamber could exhibit obstacle vortex shedding due to grain separators, inhibitor ring, non-uniform burn of propellant, or other protrusions. Considering the same rocket chamber, angle vortex shedding results from injectant entry at an angle due to lack of propellant uniformity. Finally, flow investigations of a rocket are concerned with parietal vortex shedding as it is found to initiate pressure oscillations in experimental studies using cold-gas by Prévost et al. [2], small scale motor firings [3], and simulations by Vétel et al. [4]. This type of vortex shedding is characterized by internal pressure oscillations occurring near the surface and diminishing near the centerline.

Using linear stability analysis, a higher order unsteady term is superimposed with the steady mean flow. The resulting instantaneous flow is the sum of the unsteady and steady parameters. The unsteady term can be further decomposed to three fundamental types of fluid wave motion. These are the compressible, irrotational acoustic wave, the rotational incompressible vortical wave, and the hydrodynamic wave. The first waves are commonly combined to form the vorticoacousitc wave. The vorticoacousitc wave is well known and has been studied without and with wall injection [5-11].

1.2 Hydrodynamic Instability

Hydrodynamic instability is the breakdown of the flowfield associated with vortex shedding and can result in turbulent flow. Unlike its counterpart, the vorticoacousitc wave, the hydrodynamic wave evolves over a wide spectrum of frequencies and length scales. For this reason, spectral methods are best suited to capture the flowfield and circular frequency in terms of the generalized eigenvalue problem represented by the eigenvectors and eigenvalues respectively. The pioneering studies utilizing hydrodynamic stability analysis were performed by Varapaev and Yagodkin wherein the stream function is perturbed to solve the Orr-Sommerfeld equation [12]. The one-dimensional normal mode approach was utilized in this study which assumes parallel flow, thus neglecting variations in the transverse direction [13]. Casalis et al. [14] addressed the parallel flow assumption by utilizing a technique known as the Local Nonparallel (LNP) approach. Unlike the normal mode approach which assumes all fluctuating parameters in the axial and tangential directions are zero, the LNP approach assumes them to be relatively small compared to the radial direction. This technique extended the normal mode approach to a larger range of mean flows and showed favorable comparisons to experimental data collected from VECLA and VALDO cold-flow experiments [14-19]. However, the assumption that axial and tangential parameters are relatively small compared to the radial is violated for the classic Taylor-Culick [20, 21] mean flow. In particular, the assumption of local parallel flow at the headwall and sidewall is subject to debate.

Further advancing hydrodynamic stability analysis and overcoming the local parallel assumption Theofilis [22] introduced the biglobal approach. The biglobal approach allows for significant parameter variations in radial as well as axial directions with periodic variations in the tangential direction. By allowing the amplitude function to be two dimensional the shape of the wave is not restricted to the traditional sinusoidal form. Additionally, this approach produces a system of partial differential equations which allows the satisfaction of boundary conditions at the headwall. Chedevergne et al. [19] have utilized this approach to extract the Taylor-Culick amplified modes and showed favorable comparison to VALDO experimental results. Also utilizing this approach Batterson and Majdalani [23, 24] and Elliott et al. [25] captured hydrodynamic structures in the bidirectional vortex rocket engine and in hybrid rockets with injecting headwalls respectively. The biglobal frame work utilized by Batterson [26], Batterson and Majdalani [23, 24], and Elliott et al. [25] was extended by Akiki [27] to include compressibility effects. The present work aims to extend the same framework to include two-phase flows where particles are injected with the propellant.

1.3 Stability Criteria and Illustration

A dynamic system is considered stable if the fluctuating parameters are decaying with time to some acceptable value. This stability criteria is known as Lyapunov Stability, named after Aleksandr Lyapunov, and it can be generally defined for the nonlinear dynamic system , $\dot{x} = f\left(x(t)\right)$, as follows [28-30]:

$$\left\| x(t) - x_e \right\| < \varepsilon \quad \text{for} \quad t \geq 0$$

where $x(t)$ is the system state vector, x_e is an equilibrium where $f\left(x_e\right) = 0$, and ε is a user specified distance from the equilibrium. Within this study the criteria for the fluctuating parameters is the following:

$$
\left.\begin{array}{l}
\left\|u_r(r,\theta,z,t)\right\|, \quad \left\|u_\theta(r,\theta,z,t)\right\|, \quad \left\|u_z(r,\theta,z,t)\right\|, \\
\left\|u_{rP}(r,\theta,z,t)\right\|, \quad \left\|u_{\theta P}(r,\theta,z,t)\right\|, \quad \left\|u_{zP}(r,\theta,z,t)\right\|, \\
\left\|x_P(r,\theta,z,t)\right\|, \quad \left\|p(r,\theta,z,t)\right\|
\end{array}\right\} \to 0 \text{ as } t \to \infty
$$

Now that the stability criteria for the individual fluctuating parameters have been defined it is beneficial to discuss the global stability in terms of primary results for the method utilized in this work, eigenvalues. The eigenvalues associated with each problem are plotted over the entire spectrum, as illustrated in Figure 1.1. These spectra can be viewed in terms of stability, similar to a typical Hopf bifurcation where the problem is considered stable when the imaginary component, specifically a part of this component termed the first Lyapunov coefficient, of the frequency is negative [31]. In Figure 1.1 the horizontal line demonstrates the dividing line between regions of stable (below the line) and unstable (above the line) eigenvalues. The results throughout this work will be primarily focused on the values in the unstable region.

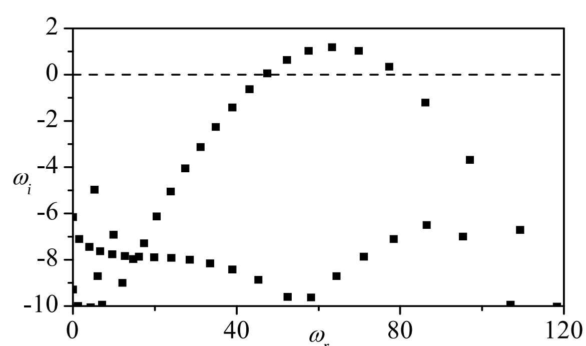

Figure 1.1: Example of spectrum for a simulated solid rocket with horizontal line dividing the unstable region $(\omega_i > 0)$ from the stable region $(\omega_i \leq 0)$

1.4 Particle Entrainment

Particle-laden flow and its stability characteristics have been a topic of interest in the propulsion and fluid dynamics communities for many years [32-46]. The injection of particles with the primary propellant can be optimized to increase the specific impulse of rockets and also act as a suppression agent for high frequency instabilities. Conventional single phase stability theory was extended by Saffman [32] to include inert particles. The presence of particles tends to reduce the gas velocity, attenuating shear effects and associated instabilities. Conversely, they also present a destabilizing effect as a result of the local growth in mass, resulting in increased Reynolds number (density sensitive). Increasing the Reynolds number results in amplification of the instability growth rates found in hydrodynamic studies. From this it is understood that the global effect of particles on intrinsic instability is not obvious. Féraille and Casalis [35] using the normal mode approach applied Saffman's two-phase concept to analyze a two-dimensional non-reactive porous chamber with the planar Taylor-Culick Profile. Their work employed constant diameter spherical particles injected into the chamber and one-way coupling using the Stokes drag force, being proportional to the relative particle velocity, to couple the gaseous and particle phases. Their results show that in rocket combustion the addition of particles can either stabilize or destabilize the flow with dependence on particle injection velocity, Stokes number, and the particle mass concentration. In this work an approach similar to that of Saffman's will be utilized with the biglobal framework to investigate two-phase flow with the cylindrical Taylor-Culick profile.

1.5 Dissertation Organization

The remainder of this paper is organized as follows. In Chapter 2 the gaseous and particle biglobal equations are formulated. This is initiated by first illustrating the geometries under investigation including the Solid Rocket Motor (SRM), Solid Rocket Motor with reactive headwall, and Hybrid Rocket Engine (HRE). Next a brief discussion on the Stokes number and normalization is given. Then the chapter provides details on the perturbation and mean flow of each phase. Finally, the chapter is brought to a close with the selection of boundary conditions.

Numerical methods are discussed in Chapter 3 including spectral methods and eigensolvers. The spectral biglobal equations for two-phase flow are given in Chapter 4. The primary objective of this chapter is to illustrate the results and analysis performed for the present work. The results are compared with those of prior works. The main conclusions of this work and future advancements are disused in Chapter 5.

Chapter 2

Formulation of Gaseous and Particle Biglobal Equations

The formulation chapter provides the development of all governing equations required for the analysis performed in this work. Starting with an assumed geometry, the problem is described via its physical model, which leads to discussion on the implementation of a particle analysis and their predicted behavior within said model. Following this model a normalization of the Navier-Stokes equations will be presented leading to the fundamental equations governing two phase flow. Finally the mean flow and particle concentration equations combined with the biglobal ansatz give rise to the two phase biglobal equations.

2.1 Geometry

The geometry under consideration is a simplified but well-justified model of a solid rocket motor core and the hybrid flowfields as found in Figure 2.1 and Figure 2.2 respectively. The gas and particle injection schemes represent the gas, and herein, the particle flows, leaving the burning surface of the propellant in both geometries. The solid rocket motor (SRM) model can represent either a reactive headwall, with constant headwall injection, or a nonreactive headwall by setting headwall injection to zero. The headwall injection velocity for the hybrid rocket model, shown in Figure 2.2, is assumed to be specified by Berman's cosine function [47] with a maximum centerline velocity of U_0. Additionally, the headwall injection velocity can be varied to reproduce the rate of mass addition at the injector faceplate of the hybrid rocket model.

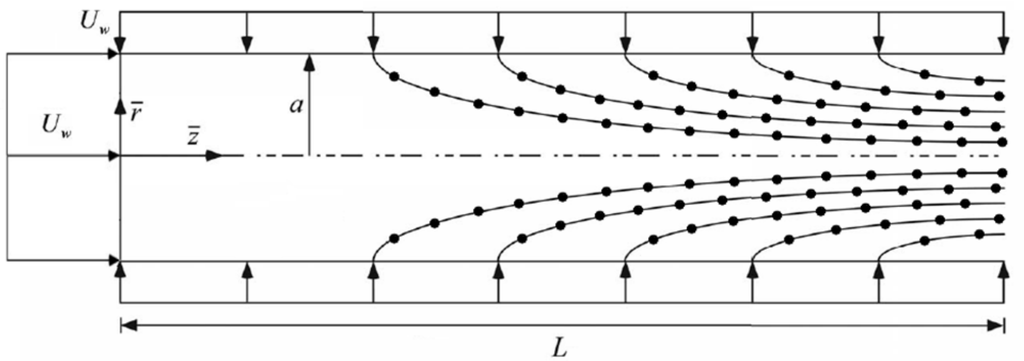

Figure 2.1: Geometry of a simulated solid rocket motor (SRM) with uniform injecting headwall and sidewall with particle entrainment

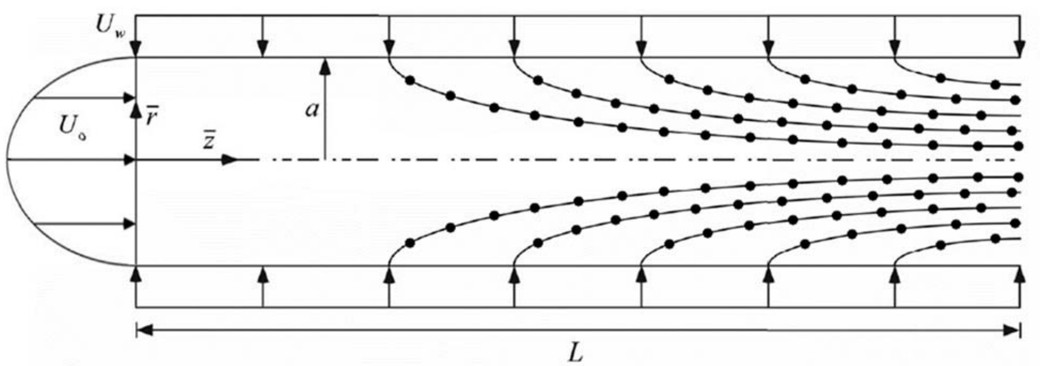

Figure 2.2: Geometry of an internal burning hybrid grain with cylindrical perforation and sinusoidally imposed headwall injection and particle entrainment.

2.2 The Stokes Number

The particle entrained flow under consideration is assumed to be incompressible with a gaseous density of ρ_G and contain particles that are spherical and chemically inert with constant diameter, d_P, a mass, m_p, and number density n_P per unit volume. The total particle mass per unit volume can be observed as $X_P = m_P n_P$. Just as Féraille and Casalis [35] this work will use the Stokes approximation to evaluate the drag force on particles. The gas density is small in comparison to the density of individual particles, justifying this approximation. The Stokes drag force on the particles is as follows:

$$\bar{\boldsymbol{F}}_S\left(\bar{r},\bar{z}\right) = 3\pi\mu d_P n_P\left[\bar{\boldsymbol{U}}_G\left(\bar{r},\bar{z}\right) - \bar{\boldsymbol{U}}_P\left(\bar{r},\bar{z}\right)\right];\; m_P = \tfrac{1}{6}\pi d_P^3 \rho_P \tag{2.1}$$

where $\bar{\boldsymbol{U}}_G = \left(\bar{U}_{rG}, \bar{U}_{zG}\right)$ and $\bar{\boldsymbol{U}}_P = \left(\bar{U}_{rP}, \bar{U}_{zP}\right)$. It is important to observe that the drag force is proportional to the number of particles and the relative velocity of the gas with respect to the entrained particles. For this expression to be valid the particle Reynolds number, Re_P, must be small, as noted below.

$$Re_P = \frac{\rho_G \left|\bar{\boldsymbol{U}}_G - \bar{\boldsymbol{U}}_P\right| d_P}{\mu} << 1 \tag{2.2}$$

The equations of motion for particles then become

$$m_P n_P \frac{\mathrm{D}\bar{\boldsymbol{U}}_P}{\mathrm{D}\bar{t}} = m_P n_P \left[\frac{\partial \bar{\boldsymbol{U}}_P}{\partial \bar{t}} + \left(\bar{\boldsymbol{U}}_P \cdot \bar{\nabla}\right)\bar{\boldsymbol{U}}_P\right] = 3\pi\mu d_P n_P \left(\bar{\boldsymbol{U}}_G - \bar{\boldsymbol{U}}_P\right) \tag{2.3}$$

The equations of motion found in Equation (2.3) can be simplified to a first-order dynamic system taking the form

$$\frac{\mathrm{D}\bar{\boldsymbol{U}}_P}{\mathrm{D}\bar{t}} + \frac{1}{\tau_P}\bar{\boldsymbol{U}}_P = \frac{1}{\tau_P}\bar{\boldsymbol{U}}_G \tag{2.4}$$

where the dynamic relaxation time is $\tau_P = \dfrac{d_P^2 \rho_P}{18\mu} = \dfrac{1}{18}\dfrac{\rho_P a^2}{\mu}\left(\dfrac{d_P}{a}\right)^2$.

It is assumed that the particles are released from rest so $\bar{\boldsymbol{U}}_P(0)=0$ and the projected time-dependent behavior is of the type

$$\bar{\boldsymbol{U}}_P(\bar{t}) \approx \bar{\boldsymbol{U}}_G\left[1-\exp\left(-\frac{\bar{t}}{\tau_P}\right)\right] \tag{2.5}$$

From this approximation the role of τ_P is fully understood as the characteristic time constant for initiating particle motion, hence terming it the dynamic relaxation time. Just as this time constant is characterized so must the characteristic time constant for mass transport be characterized. Thus defining the time needed for a particle to cross the radius of the chamber, which is estimated as $\tau_A = a/U_w$ where the particles are being injected at constant velocity, U_w, from the wall. The ratio of these characteristic time scales yields the Stokes number, S, which is a measure of particle resistance to entrainment and inertia.

$$S=\frac{\tau_P}{\tau_A}=\frac{1}{18}\frac{\rho_P U_w d_P}{\mu}\left(\frac{d_P}{a}\right) \tag{2.6}$$

The Stokes number acts as a gauge to predict if the particles follow or deviate from the surrounding fluids trajectory. As S is increased the particles resist entrainment such that at very large values, $S>1$, result in particle clustering such that the particles become uncoupled from the sounding fluid. This by definition makes sense as it implies the inertia forces are greater than the drag forces entraining the particles. For this reason this study will investigate configurations where $0.001 < S < 0.1$ which depending on the particle material equates to a particle diameter range of 30 to 300 μm.

2.2 Normalization

Experience has shown that when the governing equations are converted to non-dimensional forms, important non-dimensional parameters are recovered that prove paramount to determining and guiding the characteristics of the flow solutions. The non-dimensionalization is performed as indicated below:

$$\begin{cases} r = \dfrac{\bar{r}}{a};\ \ z = \dfrac{\bar{z}}{a};\ t = \dfrac{U_w}{a}\bar{t};\ \tilde{X} = \dfrac{m_P n_P}{\rho_G};\ \tilde{p} = \dfrac{\bar{p}}{\rho_G U_w^2};\ \nabla = a\bar{\nabla}; \\ \tilde{U}_r = \dfrac{\bar{U}_{rG}}{U_w};\ \ \tilde{U}_\theta = \dfrac{\bar{U}_{\theta G}}{U_w};\ \tilde{U}_z = \dfrac{\bar{U}_{zG}}{U_w};\ \tilde{U}_{rP} = \dfrac{\bar{U}_{rP}}{U_w};\ \ \tilde{U}_{\theta P} = \dfrac{\bar{U}_{\theta P}}{U_w};\ \ \tilde{U}_{zP} = \dfrac{\bar{U}_{zP}}{U_w} \end{cases} \tag{2.7}$$

Parameters a and U_w are the radius and reference velocity, respectively, which are used to normalize the continuity, species, and momentum equations. The non-dimensional mass concentration of particles is represented here by $\tilde{X}_P$.

At this point it should be noted that in order to satisfy the momentum conservation for the two phases, the drag force for particles as noted in Equation (2.1) should be subtracted from the gaseous momentum equation such that the gaseous-phase equation of motion is

$$\rho_G \frac{\mathrm{D}\bar{\boldsymbol{U}}_G}{\mathrm{D}\bar{t}} = -\bar{\nabla}\bar{p} + \mu\bar{\nabla}^2\bar{\boldsymbol{U}}_G - 3\pi\mu d_P n_P\left(\bar{\boldsymbol{U}}_G - \bar{\boldsymbol{U}}_P\right) \tag{2.8}$$

With the gaseous-phase equation of motion, the fundamental equations for conservation of mass and momentum, based on the non-dimensional quantities defined in Equation (2.7), can be summarized as:

Gaseous Continuity $$\nabla \cdot \tilde{\boldsymbol{U}}_G = 0 \tag{2.9}$$

Particle Continuity

$$\frac{\partial \tilde{X}_P}{\partial t} + \nabla \cdot \left(\tilde{X}_P \tilde{\boldsymbol{U}}_P \right) = 0 \tag{2.10}$$

Gaseous Momentum

$$\frac{\partial \tilde{\boldsymbol{U}}_G}{\partial t} + \left(\tilde{\boldsymbol{U}}_G \cdot \nabla \right) \tilde{\boldsymbol{U}}_G = -\nabla \tilde{p} + \frac{1}{Re} \nabla^2 \tilde{\boldsymbol{U}}_G - \frac{\tilde{X}_P}{S} \left(\tilde{\boldsymbol{U}}_G - \tilde{\boldsymbol{U}}_P \right); \quad Re = \frac{\rho_G U_w a}{\mu} \tag{2.11}$$

Particle Momentum

$$\frac{\partial \tilde{\boldsymbol{U}}_P}{\partial t} + \left(\tilde{\boldsymbol{U}}_P \cdot \nabla \right) \tilde{\boldsymbol{U}}_P = \frac{1}{S} \left(\tilde{\boldsymbol{U}}_G - \tilde{\boldsymbol{U}}_P \right) \tag{2.12}$$

2.3 Perturbation

The Equations (2.9)-(2.12) are linearized to fully realize the characteristics of small disturbance wave propagations and their possible instability modes. Perturbation methods are employed to complete this linearization and are applied to the flow variables of interest. These variables are now defined as the linear sum of the mean flow and the unsteady components of the variable. Defined in general terms, for any flow variable $\tilde{M}$

$$\tilde{M} = M + m' \tag{2.13}$$

where M is the time-mean value and m' is the unsteady component. The unsteady term can be further broken down as follows

$$m' = \hat{m} + \tilde{m} + \breve{m} \tag{2.14}$$

where $\hat{m}$ is the compressible, irrotational acoustic wave, $\tilde{m}$ is the rotational, compressible vortical wave, and $\breve{m}$ is the hydrodynamic wave.

The primary interest of this work focuses on the hydrodynamic wave and therefore the only unsteady term of interest is $\breve{m}$. The other terms, vortico-acoustic wave, have been studied at length in previous works. While these waves occur at specific frequencies, the hydrodynamic waves occur over a wide spectrum of frequencies. The following sections will use the aforementioned perturbation method to develop equations for the gaseous and particle phases, respectively.

2.3.1 Gaseous Perturbation

The gaseous-phase equations are developed by normalizing Equations (2.9) and (2.11) with the parameters found in Equation (2.7). The result is the set of viscous, incompressible Navier-Stokes equations in cylindrical coordinates with hydrodynamic characteristics captured, shown to be

Continuity

$$\frac{\partial U_r}{\partial r}+\frac{U_r}{r}+\frac{1}{r}\frac{\partial U_\theta}{\partial \theta}+\frac{\partial U_z}{\partial z}+\frac{\partial \breve{u}_r}{\partial r}+\frac{\breve{u}_r}{r}+\frac{1}{r}\frac{\partial \breve{u}_\theta}{\partial \theta}+\frac{\partial \breve{u}_z}{\partial z}=0 \tag{2.15}$$

Radial Momentum

$$\begin{aligned}
&\frac{\partial U_r}{\partial t}+U_r\frac{\partial U_r}{\partial r}+\frac{U_\theta}{r}\frac{\partial U_r}{\partial \theta}-\frac{U_\theta^2}{r}+U_z\frac{\partial U_r}{\partial z}+\frac{\partial p}{\partial r}\\
&\quad+\frac{\partial \breve{u}_r}{\partial t}+U_r\frac{\partial \breve{u}_r}{\partial r}+\breve{u}_r\frac{\partial U_r}{\partial r}+\frac{U_\theta}{r}\frac{\partial \breve{u}_r}{\partial \theta}+\frac{\breve{u}_\theta}{r}\frac{\partial U_r}{\partial \theta}-\frac{2U_\theta\breve{u}_\theta}{r}+U_z\frac{\partial \breve{u}_r}{\partial z}+\breve{u}_z\frac{\partial U_r}{\partial z}+\frac{\partial \breve{p}}{\partial r}\\
&\quad+\breve{u}_r\frac{\partial \breve{u}_r}{\partial r}+\frac{\breve{u}_\theta}{r}\frac{\partial \breve{u}_r}{\partial \theta}-\frac{\breve{u}_\theta^2}{r}+\breve{u}_z\frac{\partial \breve{u}_r}{\partial z}\\
&=\frac{1}{Re}\left(\frac{\partial^2 U_r}{\partial r^2}+\frac{1}{r}\frac{\partial U_r}{\partial r}-\frac{U_r}{r^2}+\frac{1}{r^2}\frac{\partial^2 U_r}{\partial \theta^2}-\frac{2}{r^2}\frac{\partial U_\theta}{\partial \theta}+\frac{\partial^2 U_r}{\partial z^2}+\frac{\partial^2 \breve{u}_r}{\partial r^2}+\frac{1}{r}\frac{\partial \breve{u}_r}{\partial r}-\frac{\breve{u}_r}{r^2}+\frac{1}{r^2}\frac{\partial^2 \breve{u}_r}{\partial \theta^2}\right.\\
&\quad\left.-\frac{2}{r^2}\frac{\partial \breve{u}_\theta}{\partial \theta}+\frac{\partial^2 \breve{u}_r}{\partial z^2}\right)-\frac{X_P}{S}\left(U_r-U_{rP}+\breve{u}_r-\breve{u}_{rP}\right)-\frac{\breve{x}_P}{S}\left(U_r-U_{rP}\right)-\frac{\breve{x}_P}{S}\left(\breve{u}_r-\breve{u}_{rP}\right)
\end{aligned} \tag{2.16}$$

Tangential Momentum

$$\frac{\partial U_\theta}{\partial t}+U_r\frac{\partial U_\theta}{\partial r}+\frac{U_\theta}{r}\frac{\partial U_\theta}{\partial \theta}+\frac{U_\theta U_r}{r}+U_z\frac{\partial U_\theta}{\partial z}+\frac{1}{r}\frac{\partial p}{\partial \theta}$$
$$+\frac{\partial \breve{u}_\theta}{\partial t}+U_r\frac{\partial \breve{u}_\theta}{\partial r}+\breve{u}_r\frac{\partial U_\theta}{\partial r}+\frac{U_\theta}{r}\frac{\partial \breve{u}_\theta}{\partial \theta}+\frac{\breve{u}_\theta}{r}\frac{\partial U_\theta}{\partial \theta}+\frac{U_\theta \breve{u}_r}{r}+\frac{U_r \breve{u}_\theta}{r}+U_z\frac{\partial \breve{u}_\theta}{\partial z}+\breve{u}_z\frac{\partial U_\theta}{\partial z}+\frac{1}{r}\frac{\partial \breve{p}}{\partial \theta}$$
$$+\breve{u}_r\frac{\partial \breve{u}_\theta}{\partial r}+\frac{\breve{u}_\theta}{r}\frac{\partial \breve{u}_\theta}{\partial \theta}+\frac{\breve{u}_r\breve{u}_\theta}{r}+\breve{u}_z\frac{\partial \breve{u}_\theta}{\partial z}$$
$$=\frac{1}{Re}\left(\frac{\partial^2 U_\theta}{\partial r^2}+\frac{1}{r}\frac{\partial U_\theta}{\partial r}-\frac{U_\theta}{r^2}+\frac{1}{r^2}\frac{\partial^2 U_\theta}{\partial \theta^2}+\frac{2}{r^2}\frac{\partial U_r}{\partial \theta}+\frac{\partial^2 U_\theta}{\partial z^2}+\frac{\partial^2 \breve{u}_\theta}{\partial r^2}+\frac{1}{r}\frac{\partial \breve{u}_\theta}{\partial r}-\frac{\breve{u}_\theta}{r^2}+\frac{1}{r^2}\frac{\partial^2 \breve{u}_\theta}{\partial \theta^2}\right.$$
$$\left.+\frac{2}{r^2}\frac{\partial \breve{u}_r}{\partial \theta}+\frac{\partial^2 \breve{u}_\theta}{\partial z^2}\right)-\frac{X_P}{S}\left(U_\theta-U_{\theta P}+\breve{u}_\theta-\breve{u}_{\theta P}\right)-\frac{\breve{x}_P}{S}\left(U_\theta-U_{\theta P}\right)-\frac{\breve{x}_P}{S}\left(\breve{u}_\theta-\breve{u}_{\theta P}\right) \quad (2.17)$$

Axial Momentum

$$\frac{\partial U_z}{\partial t}+U_r\frac{\partial U_z}{\partial r}+\frac{U_\theta}{r}\frac{\partial U_z}{\partial \theta}+U_z\frac{\partial U_z}{\partial z}+\frac{\partial p}{\partial z}$$
$$+\frac{\partial \breve{u}_z}{\partial t}+U_r\frac{\partial \breve{u}_z}{\partial r}+\breve{u}_r\frac{\partial U_z}{\partial r}+\frac{U_\theta}{r}\frac{\partial \breve{u}_z}{\partial \theta}+\frac{\breve{u}_\theta}{r}\frac{\partial U_z}{\partial \theta}+U_z\frac{\partial \breve{u}_z}{\partial z}+\breve{u}_z\frac{\partial U_z}{\partial z}+\frac{\partial \breve{p}}{\partial z}$$
$$+\breve{u}_r\frac{\partial \breve{u}_z}{\partial r}+\frac{\breve{u}_\theta}{r}\frac{\partial \breve{u}_z}{\partial \theta}+\breve{u}_z\frac{\partial \breve{u}_z}{\partial z}$$
$$=\frac{1}{Re}\left(\frac{\partial^2 U_z}{\partial r^2}+\frac{1}{r}\frac{\partial U_z}{\partial r}+\frac{1}{r^2}\frac{\partial^2 U_z}{\partial \theta^2}+\frac{\partial^2 U_z}{\partial z^2}+\frac{\partial^2 \breve{u}_z}{\partial r^2}+\frac{1}{r}\frac{\partial \breve{u}_z}{\partial r}+\frac{1}{r^2}\frac{\partial^2 \breve{u}_z}{\partial \theta^2}+\frac{\partial^2 \breve{u}_z}{\partial z^2}\right)$$
$$-\frac{X_P}{S}\left(U_z-U_{zP}+\breve{u}_z-\breve{u}_{zP}\right)-\frac{\breve{x}_P}{S}\left(U_z-U_{zP}\right)-\frac{\breve{x}_P}{S}\left(\breve{u}_z-\breve{u}_{zP}\right) \quad (2.18)$$

Further simplifying the above equations it is understood that the mean flow is known and is unaffected by the fluctuating parameters so moving forward with analysis the leading order terms $\mathcal{O}(M)$ and $\mathcal{O}(M^2)$ sum to zero. In addition, this analysis is based on solving for first order fluctuations which means further reduction can be applied by neglecting the second order terms $\mathcal{O}(\breve{m}^2)$. After applying these simplifications, Equations (2.15) – (2.18) become

Continuity

$$\frac{\partial \breve{u}_r}{\partial r}+\frac{\breve{u}_r}{r}+\frac{1}{r}\frac{\partial \breve{u}_\theta}{\partial \theta}+\frac{\partial \breve{u}_z}{\partial z}=0 \tag{2.19}$$

Radial Momentum

$$\begin{aligned}
&\frac{\partial \breve{u}_r}{\partial t}+U_r\frac{\partial \breve{u}_r}{\partial r}+\breve{u}_r\frac{\partial U_r}{\partial r}+\frac{U_\theta}{r}\frac{\partial \breve{u}_r}{\partial \theta}+\frac{\breve{u}_\theta}{r}\frac{\partial U_r}{\partial \theta}-\frac{2U_\theta \breve{u}_\theta}{r}+U_z\frac{\partial \breve{u}_r}{\partial z}+\breve{u}_z\frac{\partial U_r}{\partial z}+\frac{\partial \breve{p}}{\partial r}\\
&=\varepsilon\left(\frac{\partial^2 \breve{u}_r}{\partial r^2}+\frac{1}{r}\frac{\partial \breve{u}_r}{\partial r}-\frac{\breve{u}_r}{r^2}+\frac{1}{r^2}\frac{\partial^2 \breve{u}_r}{\partial \theta^2}-\frac{2}{r^2}\frac{\partial \breve{u}_\theta}{\partial \theta}+\frac{\partial^2 \breve{u}_r}{\partial z^2}\right)\\
&\quad-\frac{X_P}{S}\left(\breve{u}_r-\breve{u}_{rP}\right)-\frac{\breve{x}_P}{S}\left(U_r-U_{rP}\right)
\end{aligned} \tag{2.20}$$

Tangential Momentum

$$\begin{aligned}
&\frac{\partial \breve{u}_\theta}{\partial t}+U_r\frac{\partial \breve{u}_\theta}{\partial r}+\breve{u}_r\frac{\partial U_\theta}{\partial r}+\frac{U_\theta}{r}\frac{\partial \breve{u}_\theta}{\partial \theta}+\frac{\breve{u}_\theta}{r}\frac{\partial U_\theta}{\partial \theta}+\frac{U_\theta \breve{u}_r}{r}+\frac{U_r \breve{u}_\theta}{r}+U_z\frac{\partial \breve{u}_\theta}{\partial z}+\breve{u}_z\frac{\partial U_\theta}{\partial z}+\frac{1}{r}\frac{\partial \breve{p}}{\partial \theta}\\
&=\varepsilon\left(\frac{\partial^2 \breve{u}_\theta}{\partial r^2}+\frac{1}{r}\frac{\partial \breve{u}_\theta}{\partial r}-\frac{\breve{u}_\theta}{r^2}+\frac{1}{r^2}\frac{\partial^2 \breve{u}_\theta}{\partial \theta^2}+\frac{2}{r^2}\frac{\partial \breve{u}_r}{\partial \theta}+\frac{\partial^2 \breve{u}_\theta}{\partial z^2}\right)\\
&\quad-\frac{X_P}{S}\left(\breve{u}_\theta-\breve{u}_{\theta P}\right)-\frac{\breve{x}_P}{S}\left(U_\theta-U_{\theta P}\right)
\end{aligned} \tag{2.21}$$

Axial Momentum

$$\begin{aligned}
&\frac{\partial \breve{u}_z}{\partial t}+U_r\frac{\partial \breve{u}_z}{\partial r}+\breve{u}_r\frac{\partial U_z}{\partial r}+\frac{U_\theta}{r}\frac{\partial \breve{u}_z}{\partial \theta}+\frac{\breve{u}_\theta}{r}\frac{\partial U_z}{\partial \theta}+U_z\frac{\partial \breve{u}_z}{\partial z}+\breve{u}_z\frac{\partial U_z}{\partial z}+\frac{\partial \breve{p}}{\partial z}\\
&=\varepsilon\left(\frac{\partial^2 \breve{u}_z}{\partial r^2}+\frac{1}{r}\frac{\partial \breve{u}_z}{\partial r}+\frac{1}{r^2}\frac{\partial^2 \breve{u}_z}{\partial \theta^2}+\frac{\partial^2 \breve{u}_z}{\partial z^2}\right)\\
&\quad-\frac{X_P}{S}\left(\breve{u}_z-\breve{u}_{zP}\right)-\frac{\breve{x}_P}{S}\left(U_z-U_{zP}\right)
\end{aligned} \tag{2.22}$$

2.3.2 Particle Perturbation

The particle equations are developed by normalizing Equations (2.10) and (2.12) with the parameters found in Equation (2.7). The results are as set of viscous, incompressible transport equations for particle concentration, $\tilde{x}_P$, with hydrodynamic characteristics captured, shown to be

Continuity

$$\frac{\partial X_P}{\partial t}+\frac{1}{r}\frac{\partial rX_PU_{rP}}{\partial r}+\frac{1}{r}\frac{\partial X_PU_{\theta P}}{\partial \theta}+\frac{\partial X_PU_{zP}}{\partial z}$$
$$+\frac{\partial \breve{x}_P}{\partial t}+\frac{1}{r}\frac{\partial U_{rP}\breve{x}_P}{\partial r}+\frac{1}{r}\frac{\partial X_P\breve{u}_{rP}}{\partial r}+\frac{1}{r}\frac{\partial U_{\theta P}\breve{x}_P}{\partial \theta}+\frac{1}{r}\frac{\partial X_P\breve{u}_{\theta P}}{\partial \theta}+\frac{\partial U_{zP}\breve{x}_P}{\partial z}+\frac{\partial X_P\breve{u}_{zP}}{\partial z}$$
$$\frac{1}{r}\frac{\partial \breve{x}_P\breve{u}_{rP}}{\partial r}+\frac{1}{r}\frac{\partial \breve{x}_P\breve{u}_{\theta P}}{\partial \theta}+\frac{\partial \breve{x}_P\breve{u}_{zP}}{\partial z}=0 \qquad (2.23)$$

Radial Momentum

$$\frac{\partial U_{rP}}{\partial t}+U_{rP}\frac{\partial U_{rP}}{\partial r}+\frac{U_{\theta P}}{r}\frac{\partial U_{rP}}{\partial \theta}+U_{zP}\frac{\partial U_{rP}}{\partial z}$$
$$+\frac{\partial \breve{u}_{rP}}{\partial t}+U_{rP}\frac{\partial \breve{u}_{rP}}{\partial r}+\breve{u}_{rP}\frac{\partial U_{rP}}{\partial r}+\frac{U_{\theta P}}{r}\frac{\partial \breve{u}_{rP}}{\partial \theta}+\frac{\breve{u}_{\theta P}}{r}\frac{\partial U_{rP}}{\partial \theta}+U_{zP}\frac{\partial \breve{u}_{rP}}{\partial z}+\breve{u}_{zP}\frac{\partial U_{rP}}{\partial z}$$
$$+\breve{u}_{rP}\frac{\partial \breve{u}_{rP}}{\partial r}+\frac{\breve{u}_{\theta P}}{r}\frac{\partial \breve{u}_{rP}}{\partial \theta}+\breve{u}_{zP}\frac{\partial \breve{u}_{rP}}{\partial z}=\frac{1}{S}\left(U_r-U_{rP}+\breve{u}_r-\breve{u}_{rP}\right) \qquad (2.24)$$

Tangential Momentum

$$\frac{\partial U_{\theta P}}{\partial t}+U_{rP}\frac{\partial U_{\theta P}}{\partial r}+\frac{U_{\theta P}}{r}\frac{\partial U_{\theta P}}{\partial \theta}+U_{zP}\frac{\partial U_{\theta P}}{\partial z}$$
$$+\frac{\partial \breve{u}_{\theta P}}{\partial t}+U_{rP}\frac{\partial \breve{u}_{\theta P}}{\partial r}+\breve{u}_{rP}\frac{\partial U_{\theta P}}{\partial r}+\frac{U_{\theta P}}{r}\frac{\partial \breve{u}_{\theta P}}{\partial \theta}+\frac{\breve{u}_{\theta P}}{r}\frac{\partial U_{\theta P}}{\partial \theta}+U_{zP}\frac{\partial \breve{u}_{\theta P}}{\partial z}+\breve{u}_{zP}\frac{\partial U_{\theta P}}{\partial z}$$
$$+\breve{u}_{rP}\frac{\partial \breve{u}_{\theta P}}{\partial r}+\frac{\breve{u}_{\theta P}}{r}\frac{\partial \breve{u}_{\theta P}}{\partial \theta}+\breve{u}_{zP}\frac{\partial \breve{u}_{\theta P}}{\partial z}=\frac{1}{S}\left(U_\theta-U_{\theta P}+\breve{u}_\theta-\breve{u}_{\theta P}\right) \qquad (2.25)$$

Axial Momentum

$$\frac{\partial U_{zP}}{\partial t}+U_{rP}\frac{\partial U_{zP}}{\partial r}+\frac{U_{\theta P}}{r}\frac{\partial U_{zP}}{\partial \theta}+U_{zP}\frac{\partial U_{zP}}{\partial z}$$
$$+\frac{\partial \breve{u}_{zP}}{\partial t}+U_{rP}\frac{\partial \breve{u}_{zP}}{\partial r}+\breve{u}_{rP}\frac{\partial U_{zP}}{\partial r}+\frac{U_{\theta P}}{r}\frac{\partial \breve{u}_{zP}}{\partial \theta}+\frac{\breve{u}_{\theta P}}{r}\frac{\partial U_{zP}}{\partial \theta}+U_{zP}\frac{\partial \breve{u}_{zP}}{\partial z}+\breve{u}_{zP}\frac{\partial U_{zP}}{\partial z}$$
$$+\breve{u}_{rP}\frac{\partial \breve{u}_{zP}}{\partial r}+\frac{\breve{u}_{\theta P}}{r}\frac{\partial \breve{u}_{zP}}{\partial \theta}+\breve{u}_{zP}\frac{\partial \breve{u}_{zP}}{\partial z}=\frac{1}{S}\left(U_z-U_{zP}+\breve{u}_z-\breve{u}_{zP}\right) \qquad (2.26)$$

As with the gaseous equations, the mean flow parameters for particles are known and our interest is in the first order fluctuations. As such, the same simplification is applied to the particle equations, namely removal of $\mathcal{O}(M)$, $\mathcal{O}(M^2)$, and $\mathcal{O}(\breve{m}^2)$ terms. The resulting equations are

Continuity

$$\frac{\partial \breve{x}_P}{\partial t} + \frac{1}{r}\frac{\partial U_{rP}\breve{x}_P}{\partial r} + \frac{1}{r}\frac{\partial X_P\breve{u}_{rP}}{\partial r} + \frac{1}{r}\frac{\partial U_{\theta P}\breve{x}_P}{\partial \theta} + \frac{1}{r}\frac{\partial X_P\breve{u}_{\theta P}}{\partial \theta} + \frac{\partial U_{zP}\breve{x}_P}{\partial z} + \frac{\partial X_P\breve{u}_{zP}}{\partial z} = 0 \tag{2.27}$$

Radial Momentum

$$\frac{\partial \breve{u}_{rP}}{\partial t} + U_{rP}\frac{\partial \breve{u}_{rP}}{\partial r} + \breve{u}_{rP}\frac{\partial U_{rP}}{\partial r} + \frac{U_{\theta P}}{r}\frac{\partial \breve{u}_{rP}}{\partial \theta} + \frac{\breve{u}_{\theta P}}{r}\frac{\partial U_{rP}}{\partial \theta} + U_{zP}\frac{\partial \breve{u}_{rP}}{\partial z} + \breve{u}_{zP}\frac{\partial U_{rP}}{\partial z} = \frac{1}{S}\left(\breve{u}_r - \breve{u}_{rP}\right) \tag{2.28}$$

Tangential Momentum

$$\frac{\partial \breve{u}_{\theta P}}{\partial t} + U_{rP}\frac{\partial \breve{u}_{\theta P}}{\partial r} + \breve{u}_{rP}\frac{\partial U_{\theta P}}{\partial r} + \frac{U_{\theta P}}{r}\frac{\partial \breve{u}_{\theta P}}{\partial \theta} + \frac{\breve{u}_{\theta P}}{r}\frac{\partial U_{\theta P}}{\partial \theta} + U_{zP}\frac{\partial \breve{u}_{\theta P}}{\partial z} + \breve{u}_{zP}\frac{\partial U_{\theta P}}{\partial z} = \frac{1}{S}\left(\breve{u}_\theta - \breve{u}_{\theta P}\right) \tag{2.29}$$

Axial Momentum

$$\frac{\partial \breve{u}_{zP}}{\partial t} + U_{rP}\frac{\partial \breve{u}_{zP}}{\partial r} + \breve{u}_{rP}\frac{\partial U_{zP}}{\partial r} + \frac{U_{\theta P}}{r}\frac{\partial \breve{u}_{zP}}{\partial \theta} + \frac{\breve{u}_{\theta P}}{r}\frac{\partial U_{zP}}{\partial \theta} + U_{zP}\frac{\partial \breve{u}_{zP}}{\partial z} + \breve{u}_{zP}\frac{\partial U_{zP}}{\partial z} = \frac{1}{S}\left(\breve{u}_z - \breve{u}_{zP}\right) \tag{2.30}$$

2.4 Mean Flow Field

The mean flow field for this work can be divided in two overall areas, gaseous and particle. A one-way coupling between the gaseous and particle phases is utilized assuming the concentration of particles is sufficiently weak and their effects on the bulk gaseous motion can be neglected. With this assumption the mean gaseous motion can be represented by the extended Taylor-Culick solution [48]. Meanwhile the greater interest of this formulation is that of the effects of particle motion. Recent work in this area are mostly experimental studies, such as work by Cauty and Erades [49], Duprays et al. [50], and Melcher et al. [51], but a few have been simulation or model oriented [33, 52-60]. While none employ the biglobal approach to understand combustion instabilities, many have found interesting results that will prove useful in advancing this work to include other analysis [57, 58, 61]. The most noteworthy is the work by Lin [62] which could be utilized to further refine particle size within the framework found in this work. The primary means of comparison and advancement within this work is not only the advancement of an existing framework but also creating an alternate analysis method to the stream function approach in the work by Féraille and Casalis [35].

2.4.1 Gaseous Mean Flow

As mentioned in the Stokes drag section, the effects of particles on the gaseous mean flow can be ignored as it is assumed that the particle concentration is sufficiently low. In doing so, the drag forces on the gaseous motion are neglected and the remaining mean flow field is that of the extended Taylor-Culick. The self-similar form for the gaseous mean flow was found by Taylor and Culick to be

$$\begin{cases} \psi = (z+u_h)F \\ U_r = -r^{-1}F \\ U_z = (z+u_h)\pi F' \\ U_\theta = 0 \end{cases} \tag{2.31}$$

where ψ is the stream function, U is the mean flow velocity in the given direction, u_h is the headwall injection constant, and $F = \sin(\frac{1}{2}\pi r^2)$.

2.4.2 Particle Mean Flow

In order to understand the particle mean flow, knowledge can be gleaned from the works of Féraille and Casalis [35]. They found that the particle mean flow can be mathematically described by the equations:

$$\begin{cases} X_P = H(r) \\ U_{rP} = J(r) \\ U_{zP} = (z+u_h)G(r) \\ U_{\theta P} = 0 \end{cases} \tag{2.32}$$

The case investigated by Féraille and Casalis [35] was in a Cartesian coordinate system and therefore the form must be developed for to the axisymmetric case. This is achieved by applying the similarity form as shown in Equations (2.31) and (2.32) to the equation of motion for particles, as seen in Equation (2.12), in the radial direction. The r-projection of the equation of mean motion for particles is

$$U_{rP}\frac{\partial U_{rP}}{\partial r}=\frac{1}{S}\left(U_r-U_{rP}\right) \tag{2.33}$$

and expressed in terms of the similarity functions is

$$JJ'=-\frac{1}{S}\left(\frac{F}{r}+J\right) \tag{2.34}$$

This first order nonlinear ordinary differential equation yields the mean velocity of particles in the radial direction. To solve this ODE the boundary condition must be obtained. An assumption is made that injection of the particles occurs at the maximum possible injection speed into the chamber, which is the same as the gaseous injectant velocity. In this case, when particles are sufficiently small, $\bar{U}_{rP}(1)=-U_w$ or $J(1)=-1=-\phi$. In reality, the particle velocity can be varied such that it is smaller than that of the gas by some fraction, ϕ, which can be varied by two orders of magnitude based on particle mass density and the local velocity field gradient. In this work the fraction is arbitrarily varied over two orders of magnitude, $\phi=0.01, 0.03, 0.05, 0.1, 0.2, 0.4, 0.8,$ and 1.0. This formulation does yield a singularity, namely at $r=0$, so an equivalent boundary condition must be employed to circumvent this singularity while maintaining the radial inflow requirement. Approaching this by integrating from the sidewall to $r=r_1; r_1\to 0$ the singularity can be overcome. To achieve this Equation (2.34) is expanded in a Taylor series expansion such that

$$\begin{cases} J(r)=J(r_1)+(r-r_1)J'(r_1)+o\left(r-r_1\right) \\ F(r)=F(r_1)+(r-r_1)F'(r_1)+o(r-r_1) \end{cases} \tag{2.35}$$

In the limit as $r_1 \to 0$ where $J(0) = F(0) = 0$ the remaining terms of the expansion are

$$\begin{cases} J(r) = rJ'(0) + o(r) \\ F(r) = rF'(0) + o(r) \end{cases} \tag{2.36}$$

From this expansion Equation (2.34) becomes

$$J'^2(0) + \frac{J'(0)}{S} + \frac{F'(0)}{rS} = 0 \tag{2.37}$$

The positive root of Equation (2.37) is

$$J'(0) = \frac{-1 + \sqrt{1 - 4Sr^{-1}F'(0)}}{2S} \tag{2.38}$$

For this solution to be physical it must be real which occurs when

$$S \le \frac{r}{4F'(0)} \quad \text{or} \quad S \le \frac{1}{4\pi} \approx 0.0795775 \tag{2.39}$$

This provides a limit on the Stokes number associated with this analysis which aids particle assimilation with gas flow and limits any effects of particles on the gas motion.

The z-projection of the equation of motion for particles, Equation (2.12), in the axial direction is

$$U_{zP} \frac{\partial U_{zP}}{\partial z} = \frac{1}{S}\left(U_z - U_{zP}\right) \tag{2.40}$$

Just as with the velocity in the radial direction this can be written in self-similar form as

$$G^2 = \frac{1}{S}\left(\frac{F'}{r} - G\right) \quad \text{or} \quad G(r) = \frac{-1 + \sqrt{1 + 4Sr^{-1}F'(r)}}{2S} \tag{2.41}$$

2.4.2.1 Illustrations of Axisymmetric Particle Mean Velocity Components

The particle mean flow velocities were computed from Equations (2.38) and (2.41) and plotted in Figures 2.3 and 2.4 with varied Stokes number and ratio of particle-to-gas injection velocity at the sidewall. From Figure 2.3 it can be observed that the ratio of particle-to-gas injection velocity takes a secondary role to that of the Stokes number in overall flow effects. It can further be observed that the particle velocity will lag the gaseous velocity but then overtake the gaseous velocity as a result of the reduction in chamber area as the particle moves into the chamber. The gaseous velocity slows more quickly when approaching the centerline due to the ability of the gaseous flow to transfer its energy more rapidly from the radial to the axial direction through turning and integrating with the parallel stream. Particles, on the other hand, turn more gradually as Stokes number is increased in the illustrations the mean particle velocity exceeds that of the mean gaseous velocity approaching the centerline. This can be verified by Figure 2.4 where the axial velocity for particles lags that of the gaseous velocity. While a full order of magnitude is not shown in the figure, when the Stokes number is increased from $S = 0.008$ to $S = 0.08$ the maximum centerline velocity is decreased by over 22%. This reduction in velocity is another consideration for limiting the Stokes number, or particle diameter, as larger values decrease the gas velocity overall.

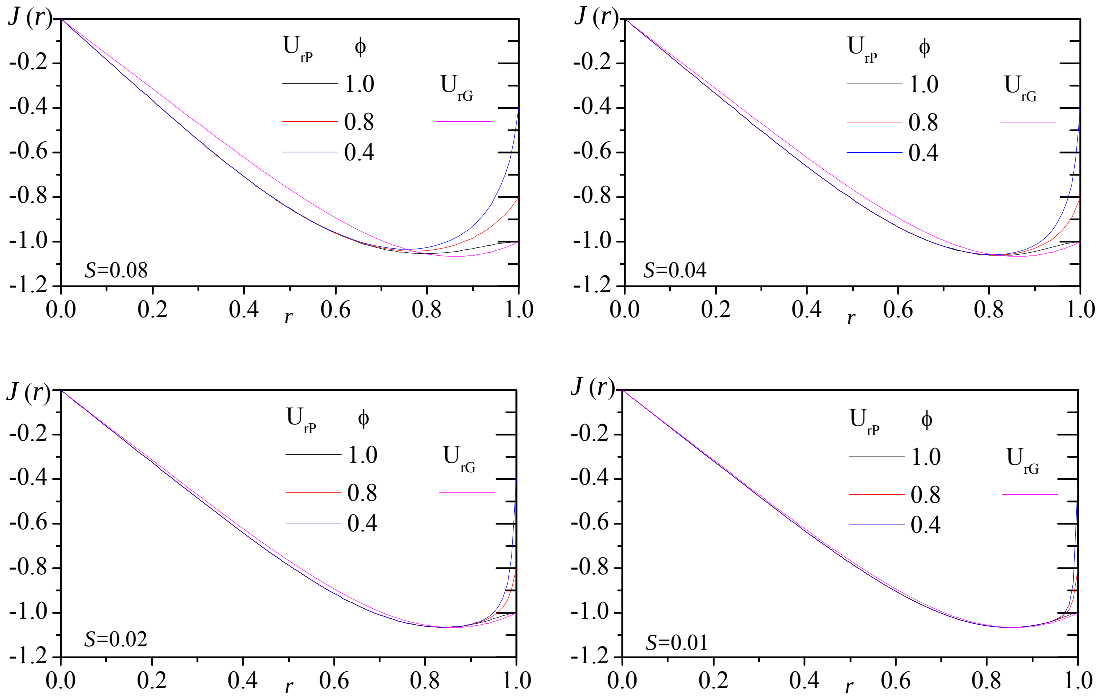

Figure 2.3: Mean radial velocities of particles and gas compared with varied stokes number and ratio of particle to gas velocity at sidewall

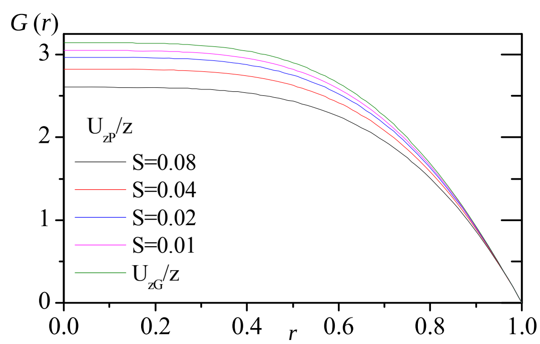

Figure 2.4: Mean axial velocities of particles and gas compared with varied stokes number and ratio of particle to gas velocity at sidewall.

2.4.2.2 Particle Concentration Field

The mean particle mass concentration, X_P, was addressed by Féraille and Casalis using the self-similar form, function of y only, as well as a general form, function of y and x, where as our work focuses only on the latter. To solve for the particle mass concentration we start with the continuity equation of particles, Equation (2.10), and assuming no tangential dependence Equation (2.10) becomes

$$U_{rP}\frac{\partial X_P}{\partial r}+U_{zP}\frac{\partial X_P}{\partial z}+\left(\frac{\partial U_{rP}}{\partial r}+\frac{U_{rP}}{r}+\frac{\partial U_{zP}}{\partial z}\right)X_P=0 \tag{2.42}$$

In practice, the rate particles enter the chamber and the mass fraction of particles must be zero at an inert headwall requiring $X_P(r,0)=X'_P(r,0)=0$. Particle mass concentration is specified along the wall as a function of z and becomes nearly equal to its asymptotic limit, $X_P(1,z)=X_{Pw}(z)=X_0$, when $z\geq z_0$. The critical abscissa where flow begins to breakdown is represented by z_0. Féraille and Casalis [35] show that particle effects are meaningful in the amplified regime downstream of z_0 and it is also known that breakdown occurs at $z_0\approx 5$ for cylindrical chambers [63]. Since the particle mass concentration and its first derivative at $z=0$ are set to zero and $X_{Pw}(z_0)$ is constant to prevent singularity at the centerline a smooth distribution is chosen for $0\leq z<z_0$. The actual shape of X_{Pw} is not known but the following piecewise function is assumed to create the smooth distribution.

$$X_{Pw}(z) = \begin{cases} \frac{1}{2} X_0 \left[1 - \cos\left(\pi z / z_0\right)\right]; & 0 \le z < z_0 \\ X_0; & z \ge z_0 \end{cases} \tag{2.43}$$

Féraille and Casalis [35] have tested two different smooth distributions representing the shape of the particle mass concentration with similar stability results near the unstable region and no variations in results downstream of the critical abscissa. Figure 2.5 shows the predicted spatial particle concentration distribution in the radial direction for different axial locations. It can be observed that axial distribution of mass concentration is reduced by decreasing particle-to-gas velocity at the side wall, ϕ. While ϕ plays the primary role in axial scattering, further analysis shows the value of S plays a limited role.

Equation (2.42) will be reduced to an ODE through the use of the method of characteristics. Again, using the self-similar form, see Equation (2.32), Equation (2.42) becomes

$$J(r)\frac{\partial X_P\left(r,z\right)}{\partial r} + \left(z + u_h\right)G(r)\frac{\partial X_P\left(r,z\right)}{\partial z} + \left[J'(r) + \frac{J(r)}{r} + G(r)\right]X_P\left(r,z\right) = 0 \tag{2.44}$$

where J, G, and $X_P(1,z) = X_{Pw}(z)$ are known.

Dividing through by J and letting $R(r) = G(r)/J(r)$, Equation (2.44) becomes

$$\frac{\partial X_P\left(r,z\right)}{\partial r} + \left(z + u_h\right)R(r)\frac{\partial X_P\left(r,z\right)}{\partial z} + \left[\frac{J'(r)}{J(r)} + \frac{1}{r} + R(r)\right]X_P\left(r,z\right) = 0 \tag{2.45}$$

To satisfy the method of characteristics, $z = z(r)$ must be chosen in a way that Equation (2.45) can be converted into an ODE. In accordance with the method a function $K(r)$ is introduced, where $K(r) = X_P\left(r, z(r)\right)$. Then $K(r)$ is differentiated with respect to r resulting in

$$K'(r) = \frac{\partial X_P}{\partial r} + z'(r)\frac{\partial X_P}{\partial z} \tag{2.46}$$

The first two terms in Equation (2.45) collapse into $K'(r)$ when $z'(r) = (z + u_h)R(r)$. This separable ODE can be integrated with the initial condition at the wall, $z(1) = z_0$, to obtain

$$z(r) = (z_0 + u_h)\exp\int_1^r \frac{G(x)}{J(x)}\mathrm{d}x - u_h \tag{2.47}$$

The original equation now reduces to

$$K'(r) + \left[\frac{J'(r)}{J(r)} + \frac{1}{r} + R(r)\right]K(r) = 0 \tag{2.48}$$

Given that $K(1) = X_P\left(1, z_0\right) = X_{Pw}(z_0)$ the general solution is

$$K(r) = K(1)\exp\left\{-\int_1^r \left[\frac{J'(x)}{J(x)} + \frac{1}{x} + R(x)\right]\mathrm{d}x\right\} = X_{Pw}(z_0)\frac{J(1)}{rJ(r)}\exp\left[-\int_1^r R(x)\mathrm{d}x\right] \tag{2.49}$$

Completing the method, Equation (2.47) is substituted into Equation (2.49) and the final solution is determined to be

$$X_P\left(r, z\right) = X_{Pw}\left[\left(z + u_h\right)I(r) - u_h\right]\frac{J(1)}{rJ(r)}I(r) \tag{2.50}$$

where

$$I(r) \equiv \exp\left[-\int_1^r \frac{G(x)}{J(x)}\mathrm{d}x\right] \tag{2.51}$$

The function $I(r)$ was numerically evaluated within the framework.

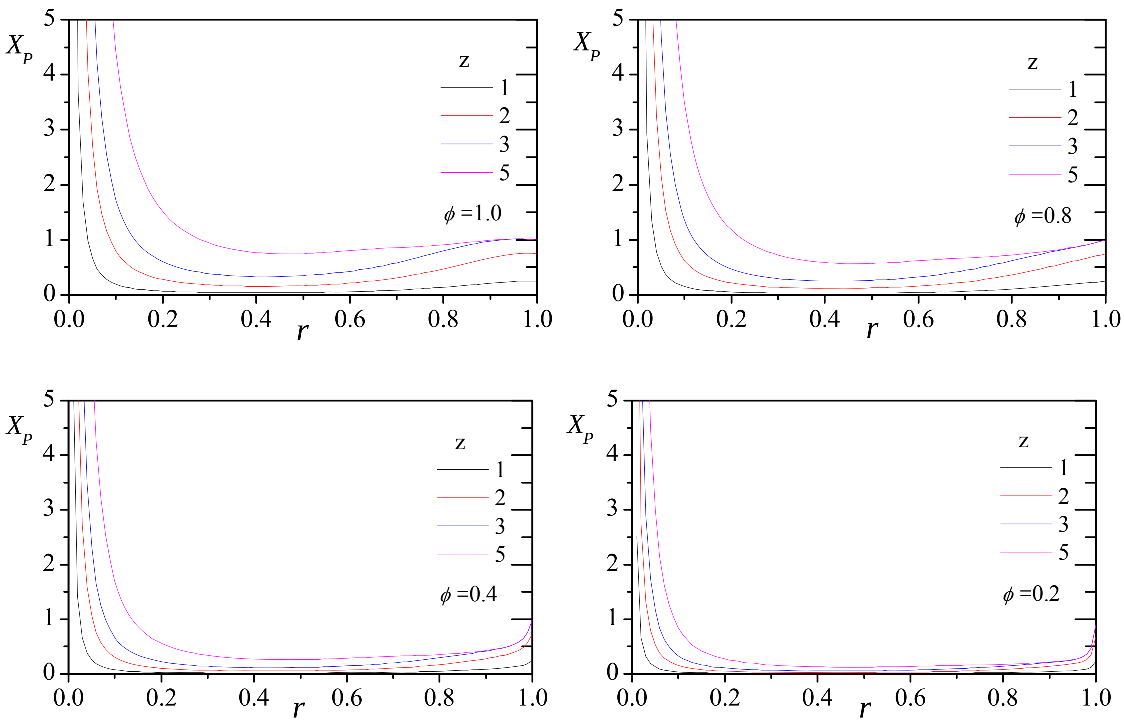

Figure 2.5: Particle mass concentration throughout the chamber with varied particle to gaseous velocity ratio and $S = 0.079$.

2.5 Boundary Conditions

The boundary conditions for the configuration under investigation must be determined to accurately assess the unsteady flow parameters and facilitate solution to the given problem. In order to illustrate the boundary conditions Figure 2.6 shows the location of the boundary conditions for the headwall $(M(r,0))$, sidewall $(M(1,z))$, centerline $(M(0,z))$, and endwall or exit plane $(M(r,Z_f))$. Starting with the gaseous equations, the no-slip condition at the sidewall is applied for mean and fluctuating velocity components. This can be observed as

$$u_r(1,z) = u_\theta(1,z) = u_z(1,z) = 0 \tag{2.52}$$

The same no slip condition can be observed at the headwall leading to

$$u_r(\mathrm{r},0) = u_\theta(\mathrm{r},0) = u_z(\mathrm{r},0) = 0 \tag{2.53}$$

The centerline is assumed to be an axis of symmetry where:

$$\frac{\mathrm{d}u_r}{\mathrm{d}r}(0,z) = u_\theta(0,z) = \frac{\mathrm{d}u_z}{\mathrm{d}r}(0,z) = \frac{\mathrm{d}p}{\mathrm{d}r}(0,z) = 0 \tag{2.54}$$

The sidewall and headwall are assumed to be acoustically closed so the pressure boundary conditions are selected as:

$$\frac{\mathrm{d}p}{\mathrm{d}r}(1,z) = \frac{\mathrm{d}p}{\mathrm{d}z}(r,0) = 0 \tag{2.55}$$

The exit conditions are selected such that hydrodynamic waves are allowed to pass through the boundary. In this case extrapolation is used in the streamwise direction [19, 22, 64]. Completing the set,

$$\frac{\mathrm{d}^2u_r}{\mathrm{d}z^2}(r,Z_f) = \frac{\mathrm{d}^2u_\theta}{\mathrm{d}z^2}(r,Z_f) = \frac{\mathrm{d}^2u_z}{\mathrm{d}z^2}(r,Z_f) = \frac{\mathrm{d}p}{\mathrm{d}z}(r,Z_f) = 0 \tag{2.56}$$

With a complete set of boundary conditions for the gaseous phase attention is turned to the boundary conditions for particle small disturbance parameters. Similar to that of the gaseous equations sufficiently small particles cannot violate the no-slip condition at the sidewall leading to Equation (2.60) and at the headwall leading to Equation (2.61)

$$u_{rP}(1,z) = u_{\theta P}(1,z) = u_{zP}(1,z) = x_P(1,z) = 0 \tag{2.57}$$

$$u_{rP}(\mathrm{r},0) = u_{\theta P}(\mathrm{r},0) = u_{zP}(\mathrm{r},0) = x_P(\mathrm{r},0) = 0 \tag{2.58}$$

Assuming symmetry across the centerline and extrapolated exit conditions the result is Equations (2.62) and (2.63) respectively.

$$\frac{\mathrm{d}u_{rP}}{\mathrm{d}r}(0,z) = u_{\theta P}(0,z) = \frac{\mathrm{d}u_{zP}}{\mathrm{d}r}(0,z) = \frac{\mathrm{d}x_P}{\mathrm{d}r}(0,z) = 0 \tag{2.59}$$

$$\frac{\mathrm{d}^2 u_{rP}}{\mathrm{d}z^2}(\mathrm{r},\mathrm{Z}_f) = \frac{\mathrm{d}^2 u_{\theta P}}{\mathrm{d}z^2}(\mathrm{r},\mathrm{Z}_f) = \frac{\mathrm{d}^2 u_{zP}}{\mathrm{d}z^2}(\mathrm{r},\mathrm{Z}_f) = \frac{\mathrm{d}x_P}{\mathrm{d}z}(\mathrm{r},\mathrm{Z}_f) = 0 \tag{2.60}$$

Equations (2.55) – (2.63) represent the complete set of boundary conditions for the geometry and flow field under consideration in this work.

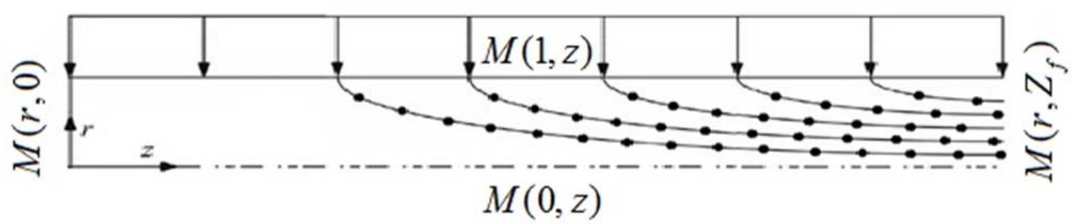

Figure 2.6: Half-chamber illustration of boundary condition locations for all parameters.

Chapter 3

Numerical Methods

The focus of this chapter is to describe the numerical methods employed to perform stability analysis of two-phase flow in solid and hybrid rockets. This work is a continuation of a stability framework first developed at UTSI by Joshua Batterson [26] which was recently advanced by Michel Akiki [27]. Due to the exhaustive measures taken by Batterson in his PhD dissertation to concisely and clearly articulate methodology and coding techniques for spectral methods, the reader is highly encouraged to review this work if the surface material offered here needs clarification. Also of interest is the work done by Trefethen [65] on spectral methods and MATLAB.

3.1 Spectral Methods

This work investigates combustion instabilities, or wave propagations, in the aforementioned geometry, to this end the eigenvalue problem with partial differential equations for the two-phase flow can be solved using several methods. The primary methods employed are the finite differencing method, the Rayleigh-Ritz-Galerkin method (or more commonly known special case, finite element method), and spectral methods. Spectral methods surpass the other methods for this case due to higher accuracy results when extended over course grids, in this case high resolution both spatially and temporally is needed to capture hydrodynamic modes. Due to the nature of some hydrodynamic modes this resolution is desirable to capture small vortex structures that drive these modes. Spectral methods have high resolution because of their global nature. This global solution is used to obtain higher order approximations which leads to the need for approximation methods. To approximate the functional solution of the two-phase governing equations, interpolating polynomials are used. Chebyshev polynomials were chosen over Legendre polynomials due to the advantageous nature of their spacing [66]. This spacing allows for higher resolution near the boundaries. A further benefit of interpolating polynomials is that they are constructed in a manner that provides an exact solution at specific points. These points are the collocation points which coincide with the zeros of the interpolating polynomial.

3.1.1 Chebyshev Polynomials

A brief overview of Chebyshev polynomials is given to aid in understanding the overall solution method. As noted above, Chebyshev polynomials are not uniformly spaced, beyond the advantages previously discussed, this also alleviates issues such as Gibb's and Runge phenomenon. The Gibb's phenomenon is the Fourier series behavior at a discontinuity associated with a piecewise continuously differentiable periodic function. Chebyshev polynomials on the other hand, have the useful features of orthogonal polynomials and the Fourier series. They are favorable because they allow for larger average squared error but reduce the maximum error over the entire computational interval of interest [66, 67]. Associated with Lagrange interpolation, the Runge phenomenon is a result of the approximations attempt to resolve oscillations at or near the intervals edge [65].

Chebyshev polynomials of the first type satisfy the differential equation

$$(1-\xi^2)T''_{N-1}(\xi)-\xi T'_{N-1}(\xi)+\mathrm{N}^2\,T_{N-1}(\xi)=0 \tag{3.1}$$

After the following change of variables:

$$\xi=\cos\theta \;\;\text{with}\;\; \frac{\mathrm{d}}{\mathrm{d}\xi}=\frac{-1}{\sin\theta}\frac{\mathrm{d}}{\mathrm{d}\theta}$$

the equation can be redefined as

$$\frac{\mathrm{d}^2T_{N-1}}{\mathrm{d}\theta^2}+(N-1)^2T_{N-1}=0 \tag{3.2}$$

The solution to this equation is

$$T_{N-1}(\xi)=\cos\left[\left(N-1\right)\arccos(\xi)\right] \tag{3.3}$$

In application these polynomials can approximate both known and unknown functions to degree N. The order N discrete polynomial approximation of the function $f(\xi)$ can be shown as

$$P_N\,f\left(\xi_N\right)=\sum_{i=1}^{N}f\left(\xi_i\right)\lambda_i(\xi) \tag{3.4}$$

where ξ_i is the collocation points and $\lambda_i(\xi)$ are the weight functions from $i=1,\ldots,N$.

The weight function takes the form [26]:

$$\lambda_i(\xi) = (-1)^i \left(\frac{1-\xi^2}{\xi-\xi_i}\right)\left[\frac{T'_{N-1}(\theta)}{\mathrm{d}_i(N-1)^2}\right] \quad \text{with} \quad \begin{cases} \xi_i = \cos\left[\dfrac{(i-1)\pi}{N-1}\right] \\ \theta = \arccos(\xi) \end{cases} \tag{3.5}$$

with

$$\mathrm{d}_i = \begin{cases} 2; & i=1 \text{ or } N \\ 1; & \text{otherwise} \end{cases} \tag{3.6}$$

Equation (3.5) yields a system of N equations and N unknowns which must be solved simultaneously to find the values of the function f at the collocation points.

3.1.2 Pseudo-Spectral Derivatives

Due to the nonuniform nature of Chebyshev collocation, resulting in sensitivity of derivative formulation to step size, a similar means for derivative approximation must be utilized. Given the polynomial approximation, $P_N f$, the first derivative of f can be approximated at the collocation nodes with the exact first derivative of $P_N f$ mapped to the interval [-1,1]. The derivative of $P_N f$ is termed the pseudo-spectral derivative found in Equation (3.7).

$$D_N f = (P_N f)' \tag{3.7}$$

Just as the original interpolating polynomial was defined the derivative can be defined as

$$D_N f(\xi_N) = \sum_{i=1}^{N} f(\xi_i)\lambda'_i(\xi) \tag{3.8}$$

The values of f can be calculated directly and the derivative of the weight functions can be calculated and stored, within the pseudo-spectral differentiation matrix, a priori. Knowing this differentiation matrix Equation (3.8) can be expressed as

$$f'_N = D_N f_N \tag{3.9}$$

This method of defining the differentiation matrix is most advantageous in that higher order derivatives can be determined by raising the differentiation matrix to the corresponding power.

3.1.3 Eigenvalue Problems

The system of PDEs for two-phase combustion analysis fit the generalized eigenvalue problem of the form

$$A_{ij} f_i = \lambda B_{ij} f_i \tag{3.10}$$

Where A_{ij} and B_{ij} are operating matrices, f_i is the eigenvector, and λ is the eigenvalue. The first step in approaching this problem is to determine the transformation to map the solution over the interval [-1,1]. In general any interval can be mapped via

$$\begin{aligned} r &= \frac{r_B}{2}(\xi+1) - \frac{r_A}{2}(\xi-1) \quad \leftrightarrow \quad \xi = \frac{2x-(\mathrm{r_B}+r_A)}{r_B - r_A} \\ z &= \frac{z_D}{2}(\eta+1) - \frac{z_C}{2}(\eta-1) \quad \leftrightarrow \quad \eta = \frac{2z-(\mathrm{z}_D+z_C)}{z_D - z_C} \end{aligned} \tag{3.11}$$

Here r_A, r_B, z_C, and z_D are the boundaries of the domain and the following is true of the partial derivatives:

$$
\begin{aligned}
\frac{\partial}{\partial r} &= \frac{2}{r_B - r_A}\frac{\partial}{\partial \xi} \\
\frac{\partial}{\partial z} &= \frac{2}{z_B - z_A}\frac{\partial}{\partial \eta}
\end{aligned} \tag{3.12}
$$

The Kronecker- or tensor- product for matrices, Equation (3.13), is used to build a single matrix from a two-dimensional collocation. In the case above the derivatives with respect to r take the form $(D_N)\otimes(\mathrm{I}_N)$ while the derivatives with respect to z take the form $(\mathrm{I}_N)\otimes(D_N)$ where (D_N) is the differentiation matrix and $(\mathrm{I}_N)$is the identity matrix.

$$
A_{ij}\otimes B_{mn} = \begin{bmatrix} a_{11}B_{mn} & \cdots & a_{1j}B_{mn} \\ \vdots & \ddots & \vdots \\ a_{i1}B_{mn} & \cdots & a_{jj}B_{mn} \end{bmatrix} \tag{3.13}
$$

The operator matrices can be built for the system of PDEs now that the differentiation matrices have been determined. For the two-phase formulation each operator matrix can be subdivided into subsets over the entire grid encompassing the coefficients of eight dependent variables in eight equations. In the case of $N\times N$ collocation points, the operator matrix A_{ij}, would consist of $64N^2\times N^2$ elements for a total of $64N^4$ within the operator matrices. These matrices can be expressed as follows

$$A_{ij}=\begin{array}{r c}
 & \begin{matrix} u_r & u_\theta & u_z & p & u_{rP} & u_{\theta P} & u_{zP} & x_P \\ \downarrow & \downarrow & \downarrow & \downarrow & \downarrow & \downarrow & \downarrow & \downarrow \end{matrix} \\
\begin{matrix} \text{Gas Cont.}\rightarrow \\ r-\text{ Gas Mom.}\rightarrow \\ \theta-\text{ Gas Mom.}\rightarrow \\ z-\text{ Gas Mom.}\rightarrow \\ \text{Particle Cont.}\rightarrow \\ r-\text{ Particle Mom.}\rightarrow \\ \theta-\text{ Particle Mom.}\rightarrow \\ z-\text{ Particle Mom.}\rightarrow \end{matrix} &
\begin{bmatrix}
A_{c,u_r} & A_{c,u_\theta} & A_{c,u_z} & A_{c,u_p} & A_{c,u_{rP}} & A_{c,u_{\theta P}} & A_{c,u_{zP}} & A_{c,x_P} \\
A_{r_G,u_r} & A_{r_G,u_\theta} & A_{r_G,u_z} & A_{r_G,u_p} & A_{r_G,u_{rP}} & A_{r_G,u_{\theta P}} & A_{r_G,u_{zP}} & A_{r_G,x_P} \\
A_{\theta_G,u_r} & A_{\theta_G,u_\theta} & A_{\theta_G,u_z} & A_{\theta_G,u_p} & A_{\theta_G,u_{rP}} & A_{\theta_G,u_{\theta P}} & A_{\theta_G,u_{zP}} & A_{\theta_G,x_P} \\
A_{z_G,u_r} & A_{z_G,u_\theta} & A_{z_G,u_z} & A_{z_G,u_p} & A_{z_G,u_{rP}} & A_{z_G,u_{\theta P}} & A_{z_G,u_{zP}} & A_{z_G,x_P} \\
A_{c_P,u_r} & A_{c_P,u_\theta} & A_{c_P,u_z} & A_{c_P,u_p} & A_{c_P,u_{rP}} & A_{c_P,u_{\theta P}} & A_{c_P,u_{zP}} & A_{c_P,x_P} \\
A_{r_P,u_r} & A_{r_P,u_\theta} & A_{r_P,u_z} & A_{r_P,u_p} & A_{r_P,u_{rP}} & A_{r_P,u_{\theta P}} & A_{r_P,u_{zP}} & A_{r_P,x_P} \\
A_{\theta_P,u_r} & A_{\theta_P,u_\theta} & A_{\theta_P,u_z} & A_{\theta_P,u_p} & A_{\theta_P,u_{rP}} & A_{\theta_P,u_{\theta P}} & A_{\theta_P,u_{zP}} & A_{\theta_P,x_P} \\
A_{z_P,u_r} & A_{z_P,u_\theta} & A_{z_P,u_z} & A_{z_P,u_p} & A_{z_P,u_{rP}} & A_{z_P,u_{\theta P}} & A_{z_P,u_{zP}} & A_{z_P,x_P}
\end{bmatrix}
\end{array}$$

$$B_{ij}=\begin{array}{r c}
 & \begin{matrix} u_r & u_\theta & u_z & p & u_{rP} & u_{\theta P} & u_{zP} & x_P \\ \downarrow & \downarrow & \downarrow & \downarrow & \downarrow & \downarrow & \downarrow & \downarrow \end{matrix} \\
\begin{matrix} \text{Gas Cont.}\rightarrow \\ r-\text{ Gas Mom.}\rightarrow \\ \theta-\text{ Gas Mom.}\rightarrow \\ z-\text{ Gas Mom.}\rightarrow \\ \text{Particle Cont.}\rightarrow \\ r-\text{ Particle Mom.}\rightarrow \\ \theta-\text{ Particle Mom.}\rightarrow \\ z-\text{ Particle Mom.}\rightarrow \end{matrix} &
\begin{bmatrix}
B_{c,u_r} & B_{c,u_\theta} & B_{c,u_z} & B_{c,u_p} & B_{c,u_{rP}} & B_{c,u_{\theta P}} & B_{c,u_{zP}} & B_{c,x_P} \\
B_{r_G,u_r} & B_{r_G,u_\theta} & B_{r_G,u_z} & B_{r_G,u_p} & B_{r_G,u_{rP}} & B_{r_G,u_{\theta P}} & B_{r_G,u_{zP}} & B_{r_G,x_P} \\
B_{\theta_G,u_r} & B_{\theta_G,u_\theta} & B_{\theta_G,u_z} & B_{\theta_G,u_p} & B_{\theta_G,u_{rP}} & B_{\theta_G,u_{\theta P}} & B_{\theta_G,u_{zP}} & B_{\theta_G,x_P} \\
B_{z_G,u_r} & B_{z_G,u_\theta} & B_{z_G,u_z} & B_{z_G,u_p} & B_{z_G,u_{rP}} & B_{z_G,u_{\theta P}} & B_{z_G,u_{zP}} & B_{z_G,x_P} \\
B_{c_P,u_r} & B_{c_P,u_\theta} & B_{c_P,u_z} & B_{c_P,u_p} & B_{c_P,u_{rP}} & B_{c_P,u_{\theta P}} & B_{c_P,u_{zP}} & B_{c_P,x_P} \\
B_{r_P,u_r} & B_{r_P,u_\theta} & B_{r_P,u_z} & B_{r_P,u_p} & B_{r_P,u_{rP}} & B_{r_P,u_{\theta P}} & B_{r_P,u_{zP}} & B_{r_P,x_P} \\
B_{\theta_P,u_r} & B_{\theta_P,u_\theta} & B_{\theta_P,u_z} & B_{\theta_P,u_p} & B_{\theta_P,u_{rP}} & B_{\theta_P,u_{\theta P}} & B_{\theta_P,u_{zP}} & B_{\theta_P,x_P} \\
B_{z_P,u_r} & B_{z_P,u_\theta} & B_{z_P,u_z} & B_{z_P,u_p} & B_{z_P,u_{rP}} & B_{z_P,u_{\theta P}} & B_{z_P,u_{zP}} & B_{z_P,x_P}
\end{bmatrix}
\end{array}$$

The final preparation of the system is complete once the boundary conditions have been implemented. This consists of rewriting the entries associated with the boundaries with the boundary values for the configuration.

3.2 Eigensolvers

Once the eigenvalue problem is fully defined all that is remaining is selection and execution of an eigensolver. The two methods most used in similar works will be discussed as well as their advantages, disadvantages, and limitations. The single matrix eigenvalue problem form, similar to Equation (3.10), will be used to demonstrate the methods of choice. The characteristic equation can be obtained by expanding the zeroed determinate of the single matrix eigenvalue problem as shown in Equation (3.14).

$$\det\,(A_{ij} - \lambda I_N) = 0 \tag{3.14}$$

The characteristic equation is used to obtain the eigenvalues. If multiplied through by B_{ij}^{-1} the generalized form can be expressed as a single matrix eigenvalue problem resulting in

$$A_{ij}B_{ij}^{-1} - \lambda B_{ij}B_{ij}^{-1} = C_{ij} - \lambda I_N = 0; \quad C_{ij} = A_{ij}B_{ij}^{-1} \tag{3.15}$$

The eigenvalues of C_{ij} are the eigenvalues of the original problem. In addition to the error incurred from computational accuracy of inverting and solving matrices, the process is computationally expensive. In light of this, other methods are of interest. Just as the above is not advantageous, from a computational expense aspect, algorithms based on similarity transformations are advantageous. The methods discussed in the following sections are the LU method, the QR method, and the Arnoldi algorithm.

3.2.1 QR and LR Methods

The QR and LR methods both utilize similarity transformations to determine all of the eigenvalues converging to a matrix where the eigenvalues are on the diagonal. The QR method [68] uses an orthogonal matrix which results in a computational benefit due to an ability to obtain the inverse via the transpose of the matrix. The QR decomposition sets

$$A_{ij} = Q_{ij} R_{ij} \tag{3.16}$$

where Q_{ij} is an orthogonal matrix and R_{ij} is an upper triangular matrix. The two-step process is as follows

$$A_{ij}^{(1)} = Q_{ij}^{(1)} R_{ij}^{(1)}$$
$$A_{ij}^{(2)} = R_{ij}^{(1)} Q_{ij}^{(1)}$$

Resulting in

$$A_{ij}^{(2)} = Q_{ij}^{(1)\mathrm{T}} A_{ij}^{(1)} Q_{ij}^{(1)} \tag{3.17}$$

The LR decomposition method is similar to the QR method except it uses eliminations with each iterative multiplication of all previous transformations [69]. Its form is

$$A_{ij} = L_{ij} R_{ij} \tag{3.18}$$

where L_{ij} is a lower triangular matrix and R_{ij} is an upper triangular matrix. In this case,

$$A_{ij}^{(1)} = L_{ij}^{(1)} R_{ij}^{(1)}; \quad A_{ij}^{(2)} = R_{ij}^{(1)} L_{ij}^{(1)} \tag{3.19}$$

where

$$R_{ij}^{(1)} = L_{ij}^{(1)^{-1}} A_{ij}^{(1)} \tag{3.20}$$

resulting in

$$A_{ij}^{(2)} = L_{ij}^{(1)^{-1}} A_{ij}^{(1)} L_{ij}^{(1)} \tag{3.21}$$

The QR method will be employed for this work due to its ability to capture small hydrodynamic structures and the entire spectrum all at once.

3.2.2 Arnoldi Algorithm

A primary choice for many stability studies, the Arnoldi algorithm [70-73] is robust and can accommodate sparse matrices most efficiently. This method does allow for computation interruption and is less computationally expensive. However it is inefficient when trying to capture the entire spectrum due to iteration about initially guessed eigenvalue and confined region for solution output. This study is primarily interested in obtaining the entire spectrum under varied conditions and therefore the Arnoldi solver will not be utilized at this time.

Chapter 4

Biglobal Stability Analysis with Particle Entrainment

In this chapter the biglobal stability analysis with particle entrainment will be applied to solid and hybrid rockets. Within this chapter the reduced gaseous and particle governing equations found in Chapter 2 will be restated with the ansatz for biglobal analysis leading to a fully realized set of biglobal equations. To follow are the results for solid and hybrid rockets with varied flow parameters as well as comparison to other two-phase flow works. The final results show that the given two-dimensional framework provided can accurately characterize the three-dimensional, axisymmetric, cylindrical flow for the suggested configuration with unquestioned agreement with other works.

4.1 Spectral Biglobal Equations

The derivation of the following equations results from Equations (2.19) – (2.22) and (2.27) – (2.30). Starting from the Linearized Navier-Stokes equations a detailed development of the two-phase biglobal equations can be found in Appendix A, the final result is given below for convenience.

Gaseous Continuity

$$\frac{\partial u_r}{\partial r}+\frac{u_r}{r}+iq\frac{u_\theta}{r}+\frac{\partial u_z}{\partial z}=0 \tag{4.1}$$

Gaseous Radial Momentum

$$-i\omega u_r + U_r \frac{\partial u_r}{\partial r} + u_r \frac{\partial U_r}{\partial r} + \frac{U_\theta q i}{r} u_r + \frac{u_\theta}{r}\frac{\partial U_r}{\partial \theta} - \frac{2U_\theta u_\theta}{r} + U_z \frac{\partial u_r}{\partial z} + u_z \frac{\partial U_r}{\partial z} + \frac{\partial \breve{p}}{\partial r}$$
$$= \varepsilon\left(\frac{\partial^2 u_r}{\partial r^2} + \frac{1}{r}\frac{\partial u_r}{\partial r} - \frac{u_r}{r^2} - \frac{q^2}{r^2}u_r - \frac{2iq}{r^2}u_\theta + \frac{\partial^2 u_r}{\partial z^2}\right)$$
$$-\frac{X_P}{S}\left(u_r - u_{rP}\right) - \frac{x_P}{S}\left(U_r - U_{rP}\right) \tag{4.2}$$

Gaseous Tangential Momentum

$$-i\omega u_\theta + U_r \frac{\partial u_\theta}{\partial r} + u_r \frac{\partial U_\theta}{\partial r} + \frac{iqU_\theta}{r} u_\theta + \frac{u_\theta}{r}\frac{\partial U_\theta}{\partial \theta} + \frac{U_\theta u_r}{r} + \frac{U_r u_\theta}{r} + U_z \frac{\partial u_\theta}{\partial z} + u_z \frac{\partial U_\theta}{\partial z} + \frac{iq}{r} p$$
$$= \varepsilon\left(\frac{\partial^2 u_\theta}{\partial r^2} + \frac{1}{r}\frac{\partial u_\theta}{\partial r} - \frac{u_\theta}{r^2} - \frac{q^2}{r^2}u_\theta + \frac{2iq}{r^2}u_r + \frac{\partial^2 u_\theta}{\partial z^2}\right)$$
$$-\frac{X_P}{S}\left(u_\theta - u_{\theta P}\right) - \frac{x_P}{S}\left(U_\theta - U_{\theta P}\right) \tag{4.3}$$

Gaseous Axial Momentum

$$-i\omega u_z + U_r \frac{\partial u_z}{\partial r} + u_r \frac{\partial U_z}{\partial r} + \frac{iqU_\theta}{r} u_z + \frac{u_\theta}{r}\frac{\partial U_z}{\partial \theta} + U_z \frac{\partial u_z}{\partial z} + u_z \frac{\partial U_z}{\partial z} + \frac{\partial p}{\partial z}$$
$$= \varepsilon\left(\frac{\partial^2 u_z}{\partial r^2} + \frac{1}{r}\frac{\partial u_z}{\partial r} - \frac{q^2}{r^2}u_z + \frac{\partial^2 u_z}{\partial z^2}\right)$$
$$-\frac{X_P}{S}\left(u_z - u_{zP}\right) - \frac{x_P}{S}\left(U_z - U_{zP}\right) \tag{4.4}$$

Particle Continuity

$$-i\omega x_P + \frac{1}{r}\left[U_{rP}x_P + X_P u_{rP} + x_P \frac{\partial U_{\theta P}}{\partial \theta} + U_{\theta P} iq x_P + X_P iq u_{\theta P} + u_{\theta P}\frac{\partial X_P}{\partial \theta}\right] + x_P \frac{\partial U_{rP}}{\partial r} + U_{rP}\frac{\partial x_P}{\partial r}$$
$$+u_{rP}\frac{\partial X_P}{\partial r} + X_P \frac{\partial u_{rP}}{\partial r} + x_P \frac{\partial U_{zP}}{\partial z} + U_{zP}\frac{\partial x_P}{\partial z} + X_P \frac{\partial u_{zP}}{\partial z} + u_{zP}\frac{\partial X_P}{\partial z} = 0 \tag{4.5}$$

Particle Radial Momentum

$$-i\omega u_{rP} + U_{rP}\frac{\partial u_{rP}}{\partial r} + u_{rP}\frac{\partial U_{rP}}{\partial r} + \frac{U_{\theta P}}{r} iqu_{rP} + \frac{u_{\theta P}}{r}\frac{\partial U_{rP}}{\partial \theta} + U_{zP}\frac{\partial u_{rP}}{\partial z} + u_{zP}\frac{\partial U_{rP}}{\partial z} = \frac{1}{S}\left(u_r - u_{rP}\right) \tag{4.6}$$

Particle Tangential Momentum

$$-i\omega u_{\theta P} + U_{rP}\frac{\partial u_{\theta P}}{\partial r} + u_{rP}\frac{\partial U_{\theta P}}{\partial r} + \frac{U_{\theta P}}{r} iqu_{\theta P} + \frac{u_{\theta P}}{r}\frac{\partial U_{\theta P}}{\partial \theta} + U_{zP}\frac{\partial u_{\theta P}}{\partial z} + u_{zP}\frac{\partial U_{\theta P}}{\partial z} = \frac{1}{S}\left(u_\theta - u_{\theta P}\right) \tag{4.7}$$

Particle Axial Momentum

$$-i\omega u_{zP} + U_{rP}\frac{\partial u_{zP}}{\partial r} + u_{rP}\frac{\partial U_{zP}}{\partial r} + \frac{U_{\theta P}}{r} iqu_{zP} + \frac{u_{\theta P}}{r}\frac{\partial U_{zP}}{\partial \theta} + U_{zP}\frac{\partial u_{zP}}{\partial z} + u_{zP}\frac{\partial U_{zP}}{\partial z} = \frac{1}{S}\left(u_z - u_{zP}\right) \tag{4.8}$$

It can be noted that if particle mean flow and fluctuating components as well as particle concentration are set to zero, meaning no presence of particles, the result is the two-dimensional Linearized Navier-Stokes Equations as used by Batterson and Majdalani [23, 24].

4.2 Selecting Number of Collocation Points

Trefethen and Theofilis show that 30 or more collocations points, N, result in adequate description of the spatial structure of the eigenfunctions [22, 65]. There are several limitations and constraints on the selection of a large number of collocation points. These are chiefly, computational memory, execution time, and computational processing itself. Specifically addressing the memory (RAM) constraints, the current framework uses about 8 Gb of memory to provide results when N is 35, about 16 Gb of memory when N is 45, and memory requirements outside of conventional desktop and workstation computers as N is increased further. Just as noted by Batterson [26] the runtime required to obtain results increases by several orders of magnitude moving from $N = 30$ to $N = 40$ with the runtimes being 10 minutes and 8 hours for each, respectively. The results were obtained with both workstation, single quad core, and server architectures, dual hex core. The resulting runtimes for these architectures were not different as a result of processing power however differences can be seen in less than quad core systems. The server architecture was able to deliver faster runtimes as a result of more available RAM. Due to these limitations this work utilizes an N of 45 for all results shown. The resulting biglobal operator matrices are $8(45)^2 \times 8(45)^2$ or $16,200 \times 16,200$ which is a total of 262,440,000 elements in each matrix.

4.3 Comparison of Results with Prior Analysis

While the primary works on particle entrainment are in Cartesian coordinates and utilize the normal mode approach there are some parallel comparisons that can be observed with the present work. Féraille and Casalis [35] made some observations in their analysis that hold true in the results presented here. One such observation is that if the mass concentration is increased for sufficiently large particle-to-gas injection speed, $\phi = 1$, the particles destabilized the flow. This is shown in Figure 4.1, which was directly removed from the work by Féraille and Casalis, where the possible evolution of the eigenvalues is noted with arrows pointing upward. This evolution indicates that the temporal growth rate is increasing with added particle mass concentration. This might be explained by the particles inability turn as quickly as the gaseous flow and thereby introducing disturbances. The current work finds a similar evolution of eigenvalues for the cylindrical SRM with inert headwall as shown in Figure 4.2.

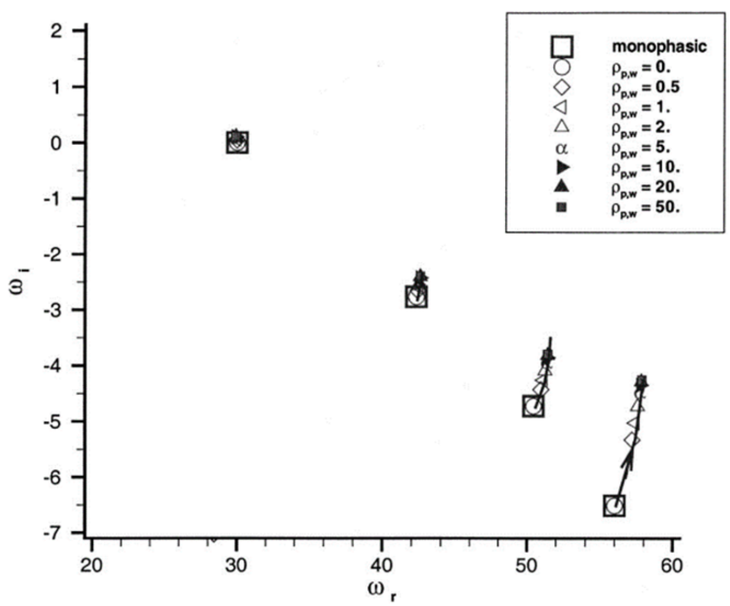

Figure 4.1: Two-phase results from Féraille and Casalis where $Re = 1000$, $S = 0.001$, $\phi = 1.0$, $u_h = 0.0$, and $q = 0$ [35].

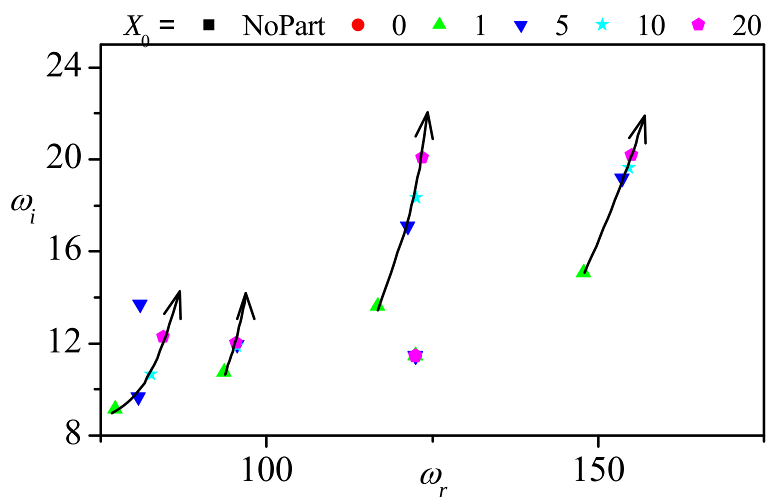

Figure 4.2: Two-phase results from the present analysis where $Re = 1000$, $S = 0.001$, $\phi = 1.0$, $u_h = 0.0$, and $q = 0$.

Also in agreement with Féraille and Casalis we find that the addition of particles has a stabilizing effect when the particle-to-gas injection speed is small, $\phi \le 0.1$, and the Stokes number is large, $S = 0.1$. This, as noted by Saffman [32], can be explained by the particles resistance to the fluctuating gaseous components as it is entrained with the bulk gaseous motion. In addition to this any gaseous fluctuations must now travel around the entrained particles which forces the dissipation of the unstable behavior. The stabilizing effects of particles can be seen in Figure 4.3 [35] for the simulated SRM. Figure 4.4 shows the results obtained for the same simulated SRM with the present framework. This figure shows that the previous framework, work by Elliott, Batterson, and Majdalani [74], agrees with the case of zero particle mass concentration. It also shows the possible evolution of eigenvalues. Again as expected when the particles are injected at a relatively low (ratio of particle to gas) velocity, the particles have a stabilizing effect on the flow. As the particle mass concentration is increased unstable modes are further suppressed. At this point it is important to note that the present framework does not account for temperature or temperature fluctuations. If the framework had this capacity the combustion temperature could be correlated with the Stokes number and particle-to-gas injection velocity, and as such the particle diameter, allowing analysis of stability and specific impulse. As noted by Huang et al. [37], there is a limit to which subsequent increases in particle diameter do not result in greater ignition temperatures. Since one of the primary ways particles increase specific impulse is through an increase in combustion temperature a balance can be determined between stability and impulse effects of particle-laden flow.

Finally, Féraille and Casalis noted that "only part of the modes" where shown in their analysis [35]. They indicate that these modes are generated by the numerical method itself and that they are not associated with the single-phase flow and were not convergent when refining the grid. This filtering of modes is not detailed and is followed by a statement that the most amplified modes are found in the single-phase analysis. This is a point of interest because in the present work the two-phase modes are more amplified depending on particle-to-gas speed and particle mass concentration

In addition to comparisons to work with particles the current framework was also used to obtain single phase results which were compared to work using the LNP approach. Figures 4.5 – 4.6 are the spectra for a simulated SRM with inert headwall $(u_h = 0)$, reactive headwall $(u_h = 0.5)$, and HRE $(u_h = 50.0)$ without particle entrainment, respectively. In these figures the axisymmetric, $q = 0$, case where $Re = 5000$ is illustrated for the solid rocket motor, $u_h = 0$, the solid rocket motor with reactive headwall, $u_h = 0.5$, and the hybrid rocket engine, $u_h = 50.0$. The threshold frequencies without particle entrainment for each of these simulated rockets are $\omega = 38.432 + 0.0287i$, $\omega = 39.7032 + 0.30657i$, and $\omega = 82.5351 + 0.3265i$ respectively.

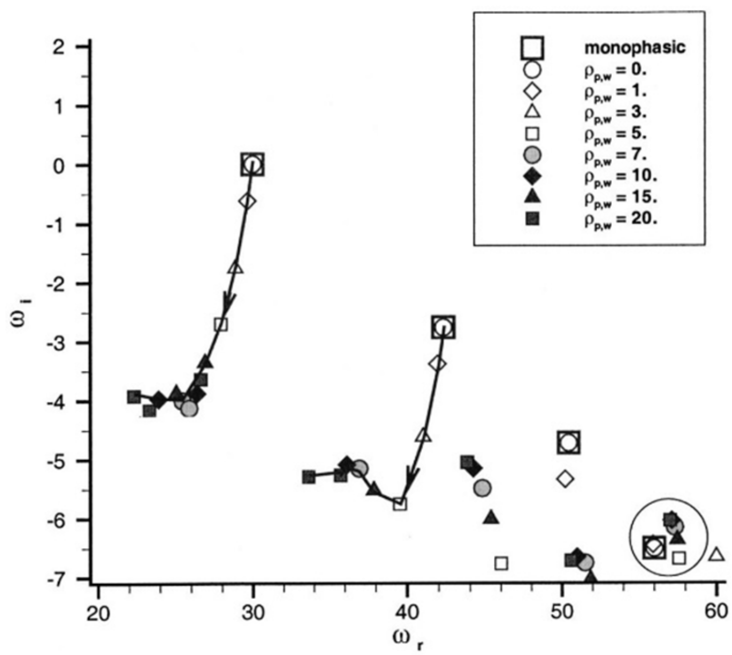

Figure 4.3: Two-phase results from Féraille and Casalis where $Re = 1000$, $S = 0.1$, $\phi = 0.1$, $u_h = 0.0$, and $q = 0$ [35].

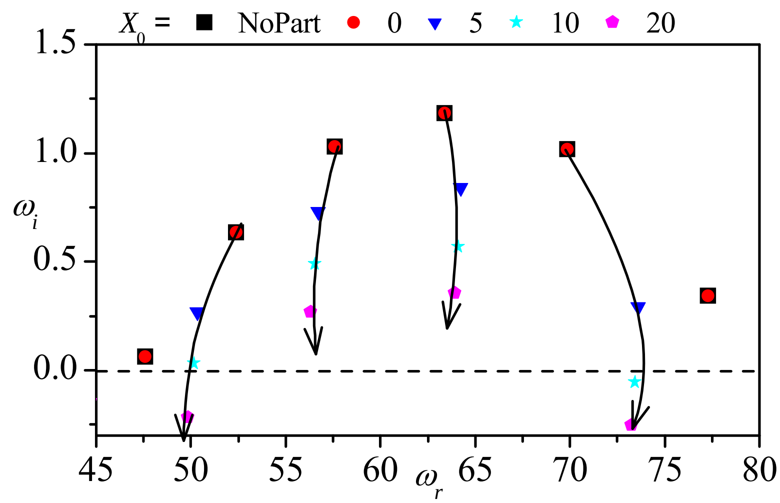

Figure 4.4: Two-phase results from the present analysis where $Re = 1000$, $S = 0.1$, $\phi = 0.1$, $u_h = 0.0$, and $q = 0$.

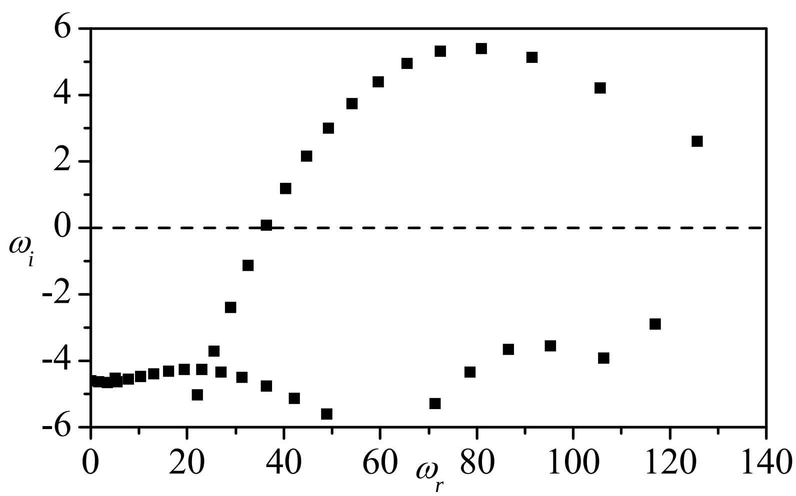

Figure 4.5: Axisymmetric spectrum for solid rocket motor without headwall injection.

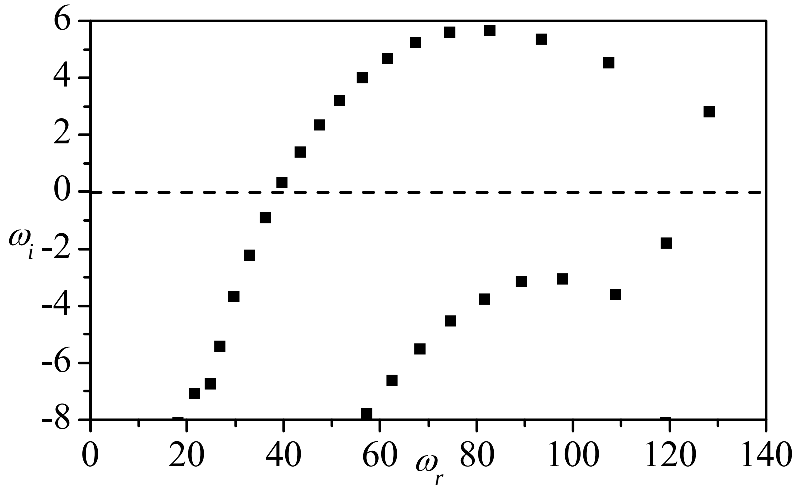

Figure 4.6: Axisymmetric spectrum for solid rocket motor with reactive headwall $u_h = 0.5$

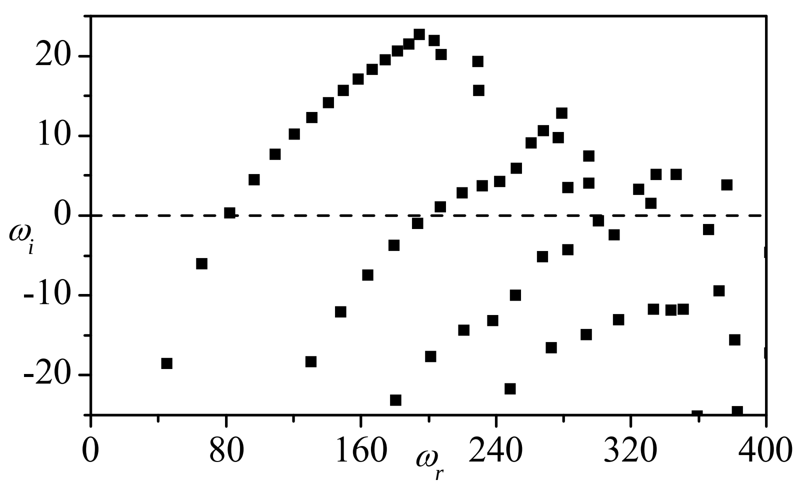

Figure 4.7: Axisymmetric spectrum for hybrid rocket motor with $u_h = 50$.

As expected for these simulations we find that as headwall injection is increased there is an increase in threshold frequency but also an increase in the range of unstable modes.

Review of work by Abu-Irshaid, Majdalani, and Casalis [15] provides insight for expected trends in threshold frequencies. When compared to the Iso-n factors, found in Figure 4.8, the results without particle entrainment shows very good agreement with this work where results are $\omega_{01} = 39.7032 + 0.30657i$, $\omega_{11} = 57.803 + 0.2085i$, $\omega_{21} = 75.888 +0.4281i$, and $\omega_{31} = 76.054 + 0.0156i$ for the cases of $q = 0,1,2,$ and 3. In Figure 4.4, from Abu-Irshaid et al, the threshold circular frequencies for the same cases above are $\omega_r = 33$, $\omega_r = 28.5$, $\omega_r = 34$, and $\omega_r = 47$. The Iso-n factors for $q = 1$ dip to a lower threshold frequency than that of $q = 0$ with a threshold of 28.5. The Iso-n factors indicate the thresholds for $q = 2$ and 3 are 34 and 47 respectively. While the threshold frequencies are not the same the overall trend between headwall injection velocity and threshold frequency and unstable range still hold true. The thresholds in the present work hold true to the expectation that the addition of particles provides a dampening effect that results in stability in a greater range of frequencies. As expected the threshold frequencies with particle entrainment are greater than those without particles and the unstable modes extend over a smaller range.

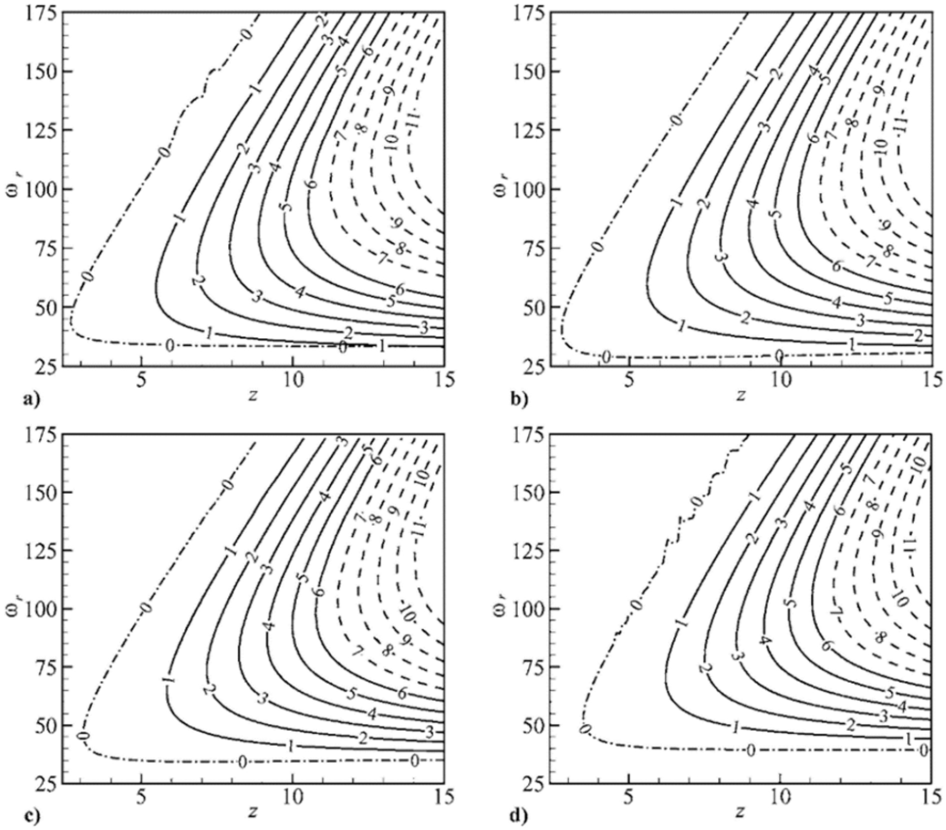

Figure 4.8: Iso-n factors from Abu-Irshaid, Majdalani, and Casalis [15] where $Re = 5000$, $u_h = 0.5$, and $q = 0$, 1, 2, and 3 in a) through d) respectively.

4.4 Biglobal Results

The parametric studies in this work start with further investigation of a simulated SRM. Turning our attention to the smooth transition we selected for the particle mass concentration at the wall, as shown in Figure 4.9, we find some interesting correlations with other numerical and experimental results [63, 75]. In this figure the smooth transition, mathematically defined in Equation (2.54), is illustrated from zero particle mass concentration at the headwall $(z=0)$ to the prescribed chamber length $(z=z_0)$ where the concentration reaches a maximum and remains constant. The eigenvalues associated with each variation in critical chamber length can be seen in Figure 4.10 along with the evolution of these values as the critical chamber length is moved further from the headwall. The destabilizing effects of transitioning the particle mass concentration

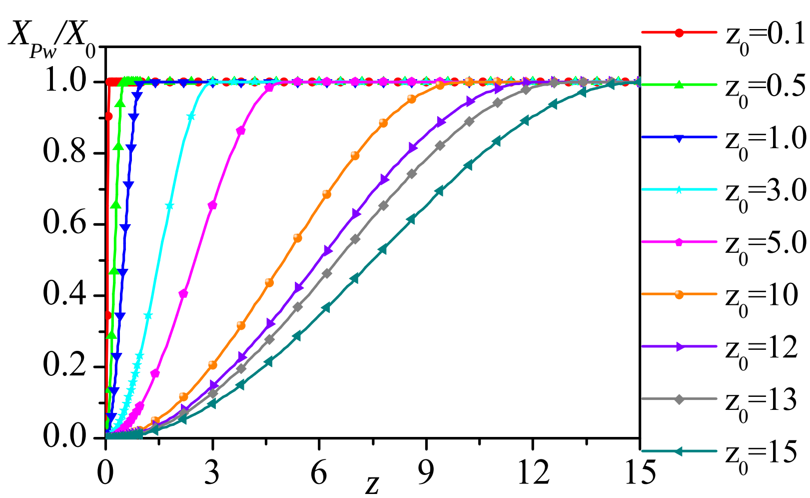

Figure 4.9: Smooth distribution of particle mass concentration to its asymptotic limit, X_0

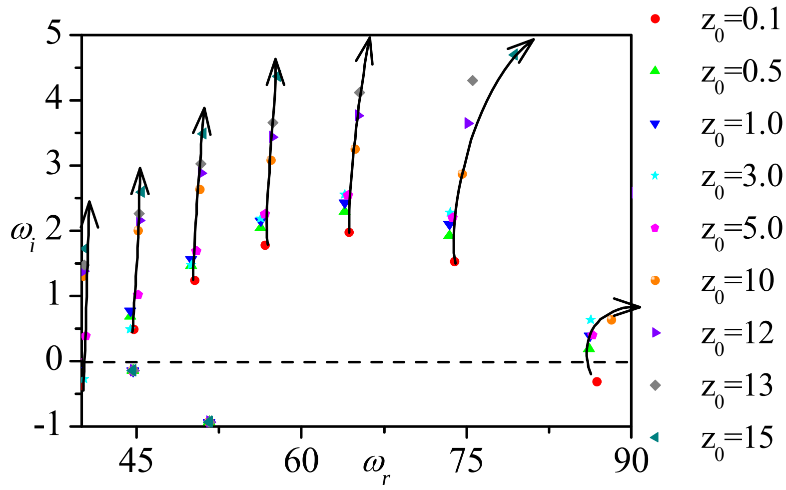

Figure 4.10: Evolution of eigenvalues as maximum particle concentration is reached at different chamber lengths.

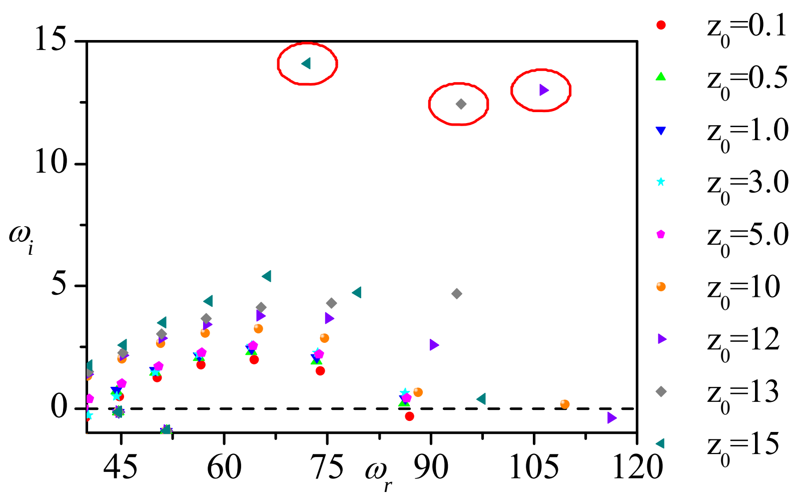

Figure 4.11: Most amplified eigenvalues as maximum particle concentration is reached at different chamber lengths.

further down the chamber are apparent and can be explained by the combination of flow breakdown and the particle transition occurring in the same area. This can be noted in the "zoomed out" version on the figure shown in Figure 4.11. Here is seen that the flow is clustered until after a critical chamber length of $z_0 = 5$, at which time the range of unstable modes increases. This can be corroborated with data obtained from the VECLA facility where Avalon et al. noted that flow begins to breakdown at 5 channel heights from the headwall, resulting in the term critical chamber length [63]. Also found in Figure 4.11 is a trend of amplified modes after a critical chamber length of $z_0 = 10$. Again, Avalon et al. found that at 10 channel heights down the chamber the flow became increasingly unstable.

Contour plots of the eigensolutions associated with the first unstable eigenvalue are found in Figure 4.12. While these plots are not particularly informative, they do illustrate some key features that indicate our results are correct. As expected the particle fluctuations are slightly smaller than that of the gaseous phase fluctuations but act in a similar manner. They are also agreeable with previous work [74] where the larger fluctuations in the radial velocity components occur along the streamlines becoming more amplified approaching the endwall, axial velocity components fluctuate throughout the entire chamber, and the most amplified pressure fluctuations occur at the endwall.

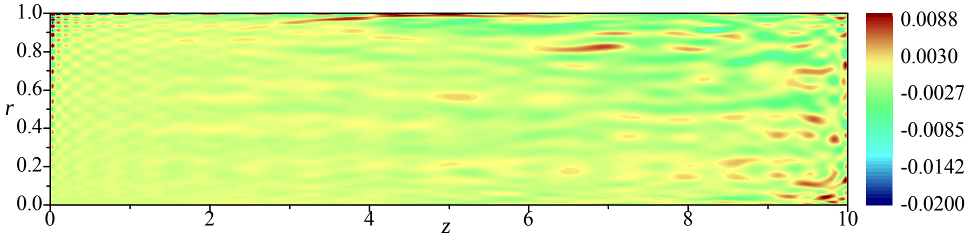

a) Gaseous radial velocity wave

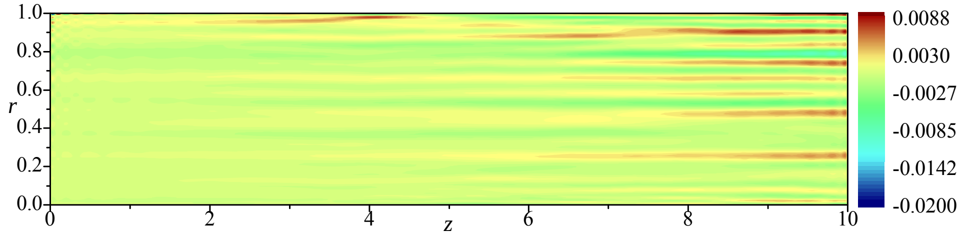

b) Gaseous axial velocity wave

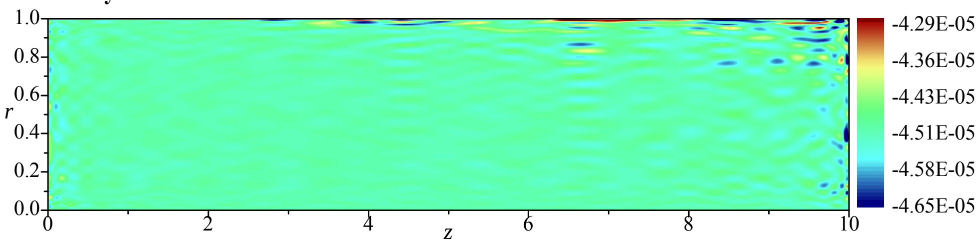

c) Pressure wave

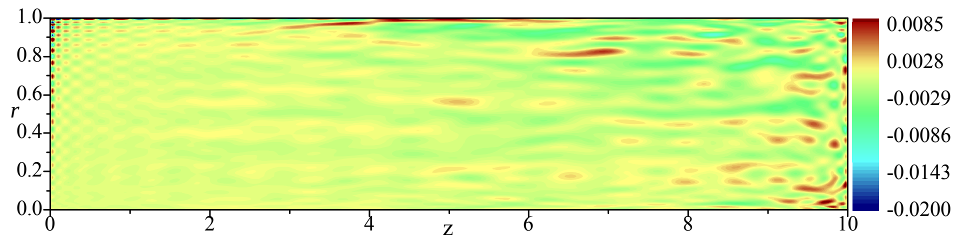

d) Particle radial velocity wave

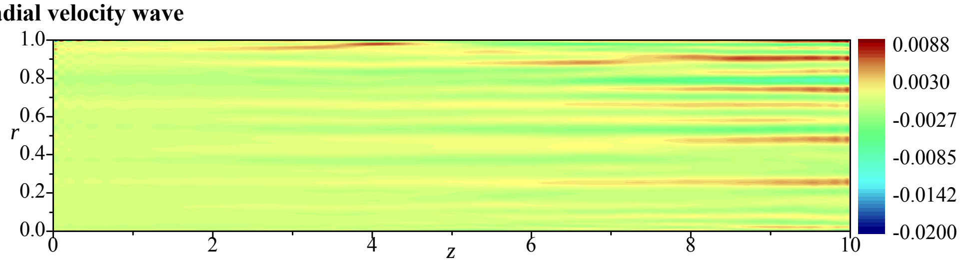

e) Particle axial velocity wave

Figure 4.12: Eigensolutions for the first unstable eigenvalue $\omega = 50.65 + 0.2469i$ with $Re = 1000$, $S = 0.1$, $\phi = 0.1$, $u_h = 0.0$, $X_0 = 5.0$, and $q = 0$.

Our attention is now turned to the simulated Solid Rocket Motor with reactive headwall. Figures 4.13 and 4.14 show results for varied particle mass concentration and low particle-to-gas injection speed and high particle-to-gas injection speed, respectively. The results are very scattered in the case of low particle-to-gas injection speed with no discernable pattern, which is counterintuitive compared to expected results and results from inert SRM. On the other hand, the results for higher particle-to-gas injection speeds appear to have a clustering trend. As would be expected the more amplified modes are in the case of higher particle-to-gas injection speeds but the clustering trend seems to indicate a maximum unstable growth rate as a result of the presences of the particles.

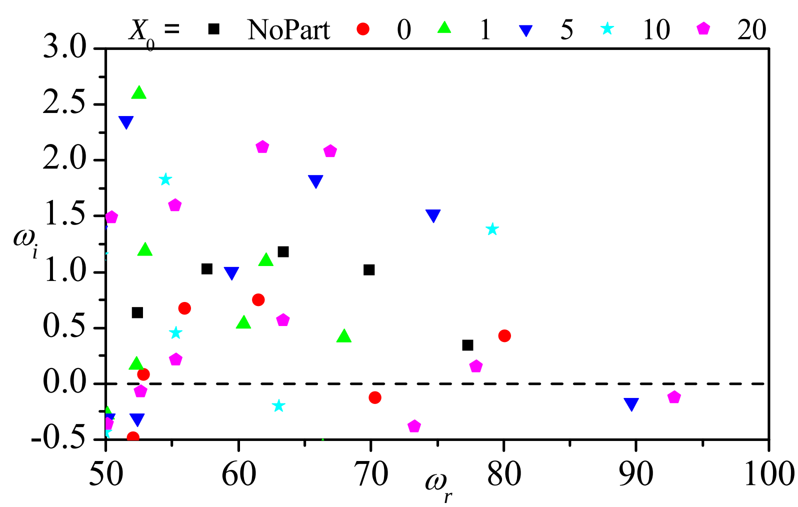

Figure 4.13: Two-phase results for a simulated solid rocket motor with reactive headwall where $Re = 1000$, $S = 0.1$, $\phi = 0.1$, $u_h = 0.5$, and $q = 0$.

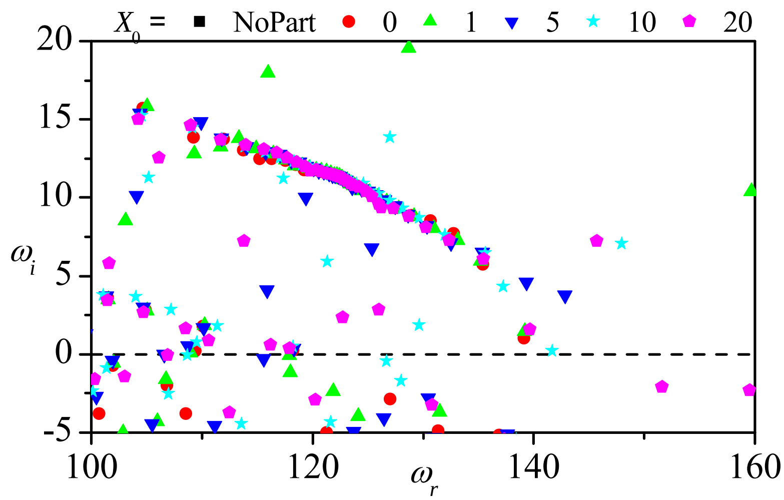

Figure 4.14: Two-phase results for a simulated solid rocket motor with reactive headwall where $Re = 1000$, $S = 0.001$, $\phi = 1.0$, $u_h = 0.5$, and $q = 0$.

Almost paradoxically, the results for the Hybrid Rocket Engine, shown in Figures 4.15 and 4.16, are exactly the opposite of those for the SRM with reactive headwall. In the HRE results the clustering trend is observed for the case of low particle-to-gas injection speed, again indicating a maximum unstable growth rate for the flow with injected particles. While the scattering of the eigenvalues shows up in the case of high particle-to-gas injection speed the overall most amplified modes are not dissimilar. Also, the range of unstable modes does not appear to increase much, relative to other simulated motors, namely the inert SRM. Both the frequency growth rate and range of unstable modes appears to be increasing with increased headwall injection which indicates our global results are trending as expected.

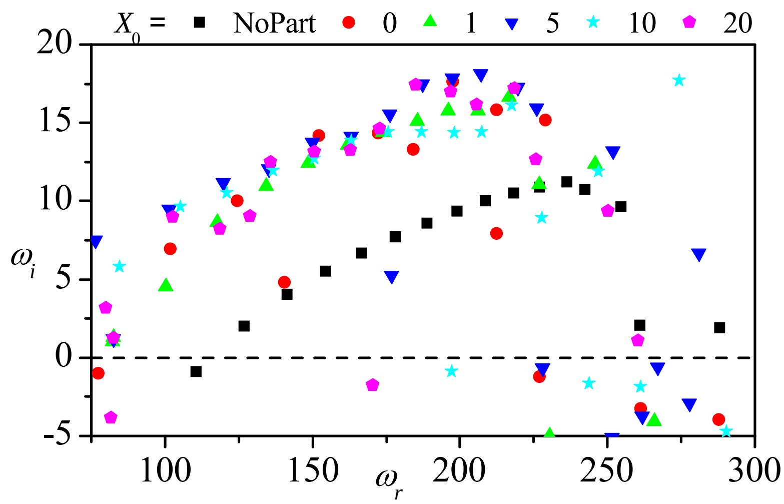

Figure 4.15: Two-phase results for a simulated hybrid rocket engine where $Re = 1000$, $S = 0.1$, $\phi = 0.1$, $u_h = 50.0$, and $q = 0$.

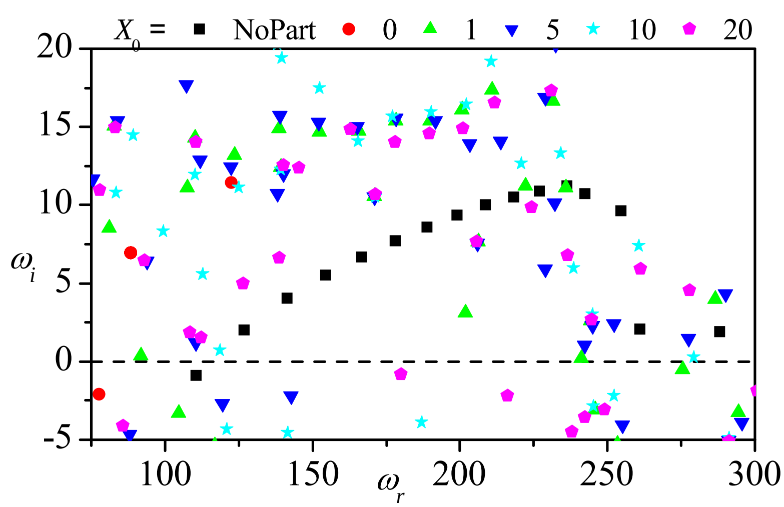

Figure 4.16: Two-phase results for a simulated hybrid rocket engine where $Re = 1000$, $S = 0.001$, $\phi = 1.0$, $u_h = 50.0$, and $q = 0$.

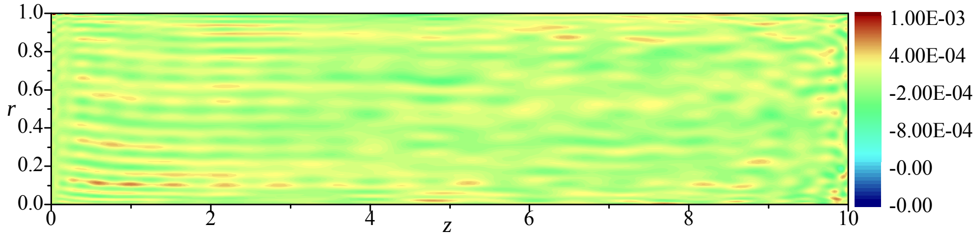

a) Gaseous radial velocity wave

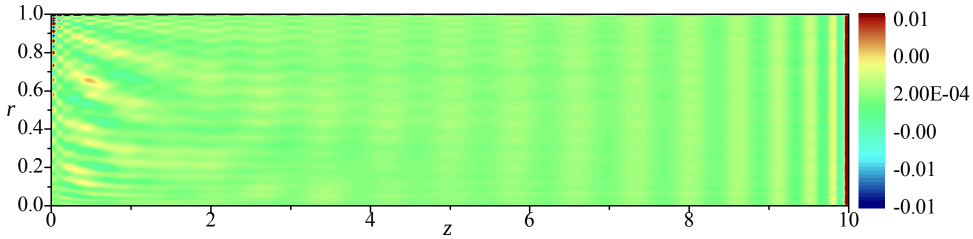

b) Gaseous axial velocity wave

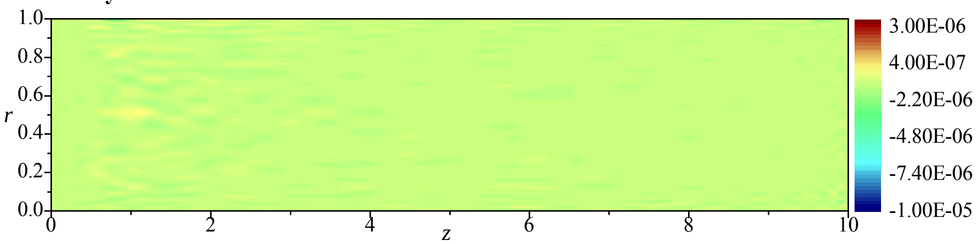

c) Pressure wave

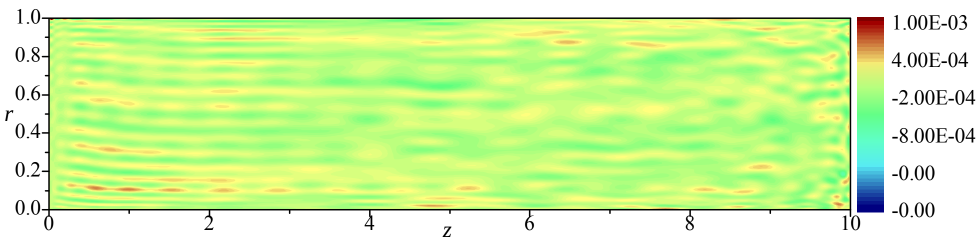

d) Particle radial velocity wave

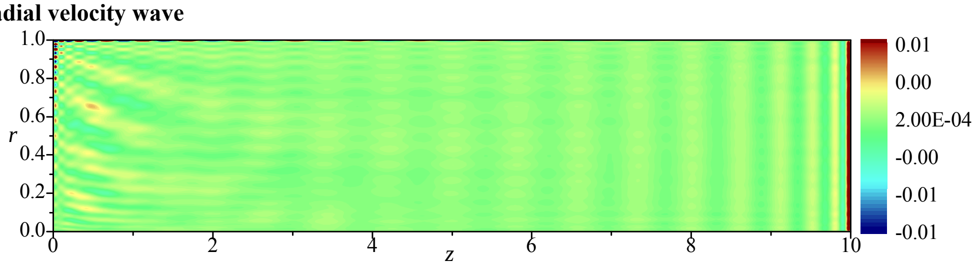

e) Particle axial velocity wave

Figure 4.17: Eigensolutions for the first unstable eigenvalue $\omega = 59.52 + 0.4958i$ with $Re = 1000$, $S = 0.1$, $\phi = 0.1$, $u_h = 50.0$, $X_0 = 5.0$, and q =0.

It appears that there may be an unexpected correlation between headwall injection velocity and the stabilizing or destabilizing effects of particles on the combustion chamber flowfield.

Just as before contour plots of the eigensolutions associated with the first unstable eigenvalue are found in Figure 4.17. Again, these contour plots do illustrate some key features that indicate our results are correct. As expected the particle fluctuations are slightly smaller than that of the gaseous phase fluctuations but act in a similar manner. They are also agreeable with previous work [74] where streamtube motion dominates throughout he chamber, the most amplified fluctuations in the radial velocity components occur along the streamlines closest to the centerline, and axial velocity component fluctuations are the greatest at the endwall. The waves associated with the eigenfunctions for the perturbed flow travel along the streamlines of the mean flow and can be observed in Figure 4.18. This figure is a representation of the velocity field for an eigenmode similar to that of analysis performed by Chedevergne et al [19], found in Figure 4.19. As noted by Chadevergne et al [19] in the area near $r = 1$ twoards the exit plane parietal vortex shedding can be observred this is the same for the current work. Furthermore, the vortex structures throughout the velocity field in Chedevergne's work can also be observed in the present work with much greater detail. The increased resolution with the present work allows for visualalization of small vortecies which are not captured in the prior work. Of course there are expected variations when comparing the two works as the presents of particles in this analysis will cause such a case.

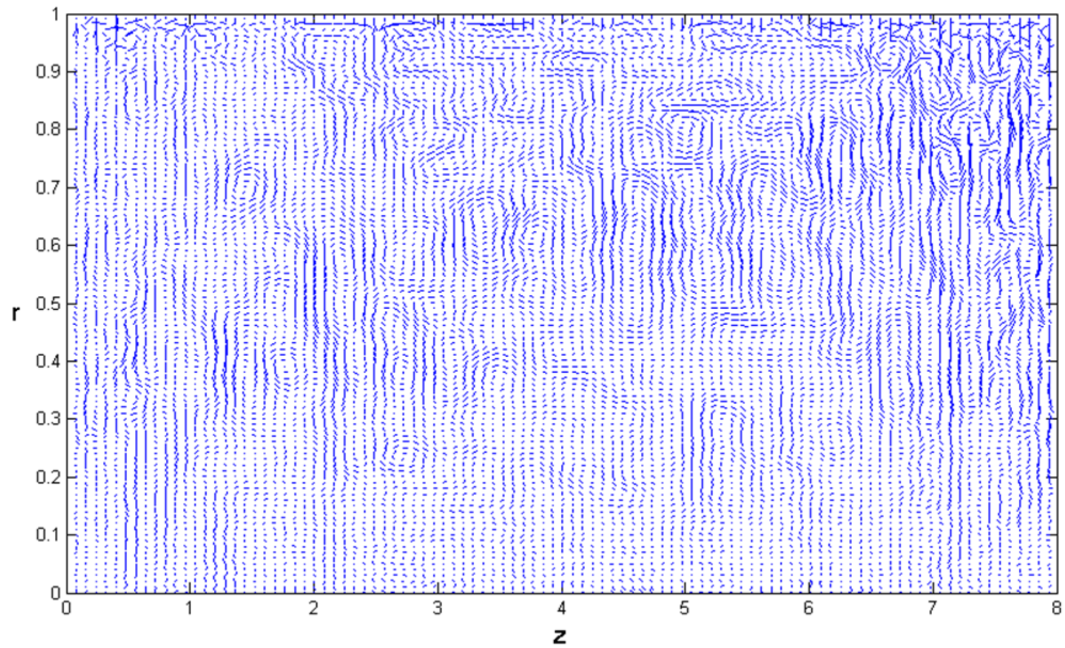

Figure 4.18: Velocity field of the eigenfunction associated with the mode $\omega_r = 63.17$ where $V_{inj} = 1.05$, $Re = 2100$, $S = 0.079$, $q = 0$, and $X_0 = 0.2$.

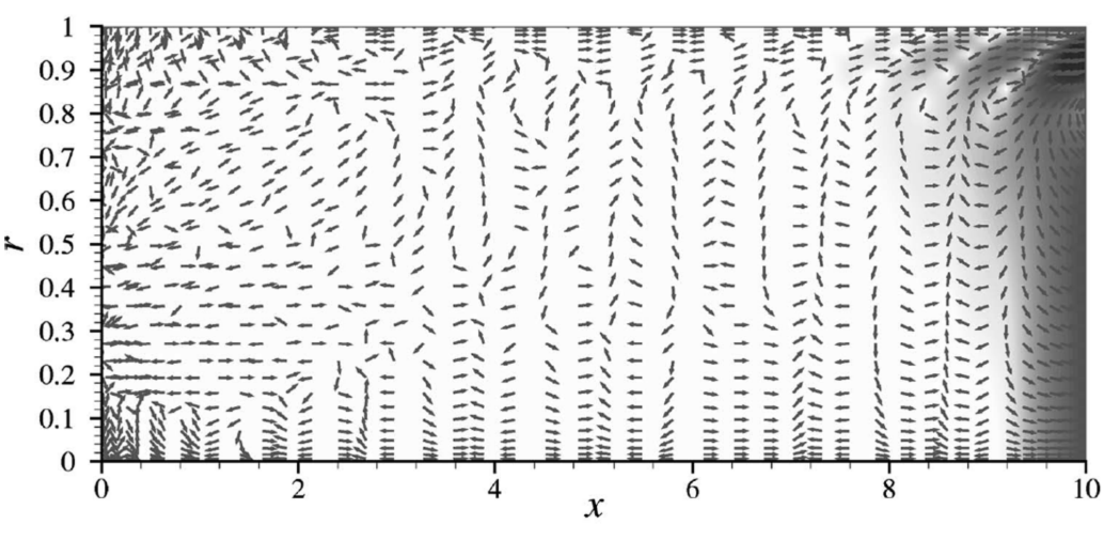

Figure 4.19: Velocity field and contours of the eigenfunction associated with the mode $\omega_r = 63.576$ where $Re = 2100$ [19].

Chapter 5

Conclusions

This dissertation advanced the biglobal framework with the inclusion of particle entrainment. The framework has been utilized to examine simulated Solid Rocket Motors with and without reactive headwalls and simulated Hybrid Rocket Engines. This work developed an analysis tool that aids in further understanding of parietal vortex shedding and associated hydrodynamic waves. This also allows one to analyze acoustic waves as vortex shedding is believed to be the triggering mechanism for hydrodynamic waves. To create this framework the equations of motion for the gaseous and particle phases are perturbed and the biglobal approach applied. Appropriate numerical procedures, such as Chebyshev collocation and spectral methods, are applied to obtain the entire spectrum of eigenvalues. The set of eigenvalues are used to prepare parametric studies of the geometries under various conditions. Consequently, the results are a means to understand the effects particle entrainment on the configurations under review.

The analysis of several configurations were compared with previous works by the author and colleagues which are, in turn, compared with works that focus on experimental cold-gas data obtained in France, specifically at the Office national d'études et de resherches aérospatiales (ONERA). The parametric studies addressing the Stokes number resulted in verification that the particles do indeed suppress oscillations in the flow. The confined physical range of the Stokes number for this formulation was found to provide the greatest frequency threshold before instabilities occur. Seemingly counter to the findings of Féraille and Casalis, we find that the two-phase flow does exhibit more amplified modes than the single-phase flow. The particle mass concentration was also considered in parametric studies showing that an elevated particle mass concentration increases the frequency threshold and stabilizes the flow, as expected: yet it also causes a diminished gaseous velocity. In connection with particle mass concentration studies, an assessment of the chamber length where the particle mass concentration reaches its maximum value was performed. The findings are compare favorably to data obtained via experimentation using rectangular test sections. A new finding in this area is the increase of the instability region when the particle mass concentration reaches its maximum at or after the point of flow breakdown. It was also found that significantly amplified, three times greater than other cases, eigenvalues occur when this maximum is reached at or after 10 radii from the headwall. The effects of variation in the azimuthal wave number are found to be comparable with previous published results. Finally, sample velocity fields were created using the current framework and compared with a sample velocity field for similar configurations without particles. The investigated vortex structures agree nicely. The presented new framework provides increased resolution in the study of vortices and related phenomena.

Future work recommendations include the investigation of the Stokes number in relation to the azimuthal wave number. This will serve the purpose of evaluating optimum versus limiting case behavior. Also further parametric analyses are suggested Reynolds number as well as expansion of current particle mass concentration to elucidate effects on flow velocity and explore implications on system stability. The studies may also lead to a quantifiable correlation between particle-to-gas injection speed and headwall injection speed. Of interest as well is the addition of particles with varying diameter. In this case, particle diameter can be utilized in rocket characterizations by the dynamic balancing of the terminal velocity and the gravitational force. The characterization with varying particle diameters would allow one to select differing particle size distributions and materials for particular configurations.

Bibliography

[1] F. Vuillot, "Vortex-shedding phenomena in solid rocket motors," *Journal of Propulsion and Power,* vol. 11, pp. 626-639, 1995.
[2] M. Prévost, J. Godon, and O. Innegraeve, "Thrust oscillations in reduced scale solid rocket motors, part I : Experimental investigations," in *AIAA*, 2005-4003, Tucson, AZ, 2005.
[3] L. Crocco, D. T. Harrje, and F. H. Reardon, "Transverse combustion instability in liquid propellant rocket motors," *Journal of the American Rocket Society,* vol. 32, p. 366, 1962.
[4] J. Vetel, Plourde, F., Doan, K. S., Prevost, M., "Cold Gas Simulations of the Influence of Inhibitor Shape in Combustor Combustion," *Journal of Propulsion and Power,* vol. 21, pp. 1098-1106, 2005.
[5] B. A. Maicke, A. Katta, and J. Majdalani, "Characterization of particle trajectories in solid rocket motors," in *AIAA*, 2013-3919, San Jose, CA, 2013.
[6] G. Flandro and J. Majdalani, "Aeroacoustic instability in rockets," *AIAA Journal,* vol. 41, pp. 485-497, February 2003.
[7] N. Zgheib and J. Majdalani, "Axial waves in simulated solid rocket motors," in *AIAA*, 2010-6993, Nashville, Tennessee, 2010.
[8] S. Fischbach and J. Majdalani, "Volume-to-surface reduction of vorticoacoustic stability integrals," *Journal of Sound and Vibration,* vol. 321, pp. 1007-1025, April 2009.
[9] C. T. Haddad and J. Majdalani, "Transverse waves in simulated liquid rocket engines," in *AIAA*, 2011-6029, San Diego, CA, 2011.
[10] C. T. Haddad and J. Majdalani, "Transverse waves in simulated liquid rocket engines with variable headwall injection," in *AIAA*, 2012-0541, Nashville, TN, 2012.
[11] C. T. Haddad and J. Majdalani, "On the sidewall boundary layer of transverse waves in simulated liquid rocket engines," in *AIAA*, 2012-4086, Atlanta, GA, 2012.
[12] V. Varapaev and V. Yagodkin, "Flow stability in a channel with porous walls," *Fluid Dynamics (Izvestiya Akademii Nauk SSSR, Meckanika Zhidkosti i Gaza),* vol. 4, pp. 91-95, 1969.
[13] F. Chedevergne, G. Casalis, and J. Majdalani, "Direct numerical simulation and biglobal stability investigations of the gaseous motion in solid rocket motors," *Journal of Fluid Mechanics,* vol. 706, pp. 190-218, September 2012.
[14] G. Casalis, G. Avalon, and J.-P. Pineau, "Spatial instability of planar channel flow with fluid injection through porous walls," *Physics of Fluids,* vol. 10, pp. 2558-2568, 1998.
[15] E. M. Abu-Irshaid, J. Majdalani, and G. Casalis, "Hydrodynamic stability of rockets with headwall injection," *Physics of Fluids,* vol. 19, pp. 024101-11, February 2007.

[16] N. Lupoglazoff and F. Vuillot, "Parietal vortex shedding as a cause of instability for long solid propellant motors. Numerical simulations and comparisons with firing tests," in *AIAA*, 96-0761, Reno, NV, 1996.

[17] N. Lupoglazoff and F. Vuillot, "Numerical simulations of parietal vortex-shedding phenomenon in a cold-flow set-up," in *AIAA*, 98-3220, Cleveland, OH, 1998.

[18] J. Griffond, "Receptivity and aeroacoustic resonance in channels with blowing walls," *Physics of Fluids,* vol. 14, pp. 3946-3962, November 2002.

[19] F. Chedevergne, G. Casalis, and T. Féraille, "Biglobal linear stability analysis of the flow induced by wall injection," *Physics of Fluids,* vol. 18, pp. 014103-14, 2006.

[20] F. Culick, "Rotational axisymmetric mean flow and damping of acoustic waves in a solid propellant rocket," *AIAA Journal,* vol. 4, pp. 1462-1464, 1966.

[21] G. Taylor, "Fluid flow in regions bounded by porous surfaces," *Proceedings of the Royal Society of London, Series A,* vol. 234, pp. 456-475, March 1956.

[22] V. Theofilis, "Advances in global linear instability analysis of nonparallel and three-dimensional flows," *Progress in Aerospace Sciences,* vol. 39, pp. 249-315, May 2003.

[23] J. W. Batterson and J. Majdalani, "Biglobal instability of the bidirectional vortex. Part 1: Formulation," in *AIAA*, 2011-5648, San Diego, CA, 2011.

[24] J. W. Batterson and J. Majdalani, "Biglobal instability of the bidirectional vortex. Part 2: Complex lamellar and Beltramian motions," in *AIAA*, 2011-5649, San Diego, CA, 2011.

[25] R. Vasilescu, "Helicopter Blade Tip Vortex Modifications in Hover Using Piezoelectrically Modulated Blowing," Ph.D., Department of Aerospace Engineering, Georgia Institute of Technology, Atlanta, GA, 2004.

[26] C. T. Haddad and J. Majdalani, "Transverse waves in simulated liquid rocket engines," *AIAA Journal,* vol. 5, pp. 591-605, March 2013.

[27] M. H. Akiki, *Multidimensional Compressible Framework for Modeling Biglobal Stability in Rocket Motors*. University of Tennessee: PhD Dissertation, 2013.

[28] M. Akiki, J. W. Batterson, and J. Majdalani, "Biglobal stability of compressible flowfields. Part 1: Planar formulation," in *AIAA*, 2013-3865, San Jose, CA, 2013.

[29] M. Akiki, J. W. Batterson, and J. Majdalani, "Biglobal stability of compressible flowfields. Part 2: Application to solid rocket motors," in *AIAA*, 2013-3866, San Jose, CA, 2013.

[30] P. G. Drazin, *Introduction to Hydrodynamic Stability*. New York, NY: Cambridge University Press, 2002.

[31] J. Majdalani and E. V. Van Horn, "Extension of the Taylor-Culick profile to rockets with noncircular grain perforations," in *AIAA*, 2013-3916, San Jose, CA, 2013.

[32] P. Saffman, "On the stability of laminar flow of a dusty gas," *Journal of Fluid Mechanics,* vol. 13, pp. 120-128, May 1962.

[33] N. X. Rao and W. K. Van Moorhem, "Interactions of particles with the flow near the burning surface of a solid propellant rocket," in *AIAA*, 93-0110, Reno, NV, 1993.
[34] S. J. Ying and C. C. Chang, "Exploratory model study of tornado-like vortex dynamics," *Journal of the Atmospheric Sciences,* vol. 27, pp. 3-14, 1970/01/01 1970.
[35] T. Féraille and G. Casalis, "Channel flow induced by wall injection of fluid and particles," *Physics of Fluids,* vol. 15, pp. 348-360, February 2003.
[36] T. S. Elliott and J. Majdalani, "Two-phase flow stability of cylindrically-shaped hybrid and solid rockets with particle entrainment," in *AIAA*, 2014-3611, Cleveland, OH, 2014.
[37] Y. Huang, G. A. Risha, V. Yang, and R. A. Yetter, "Effect of particle size on combustion of aluminum particle dust in air," *Combustion & Flame,* vol. 156, pp. 5-13, 2009.
[38] M. R. Baer and J. W. Nunziato, "A two-phase mixture theory for the deflagration-to-detonation transition (DDT) in reactive granular materials," *International Journal of Multiphase Flow,* vol. 12, pp. 861-889, 1986.
[39] I. M. Vasenin, R. K. Narimanov, A. A. Glazunov, N. E. Kuvshinov, and V. A. Ivanov, "Two-Phase flows in the nozzles of solid rocket motors," *Journal of Propulsion & Power,* vol. 11, 1995.
[40] O. A. Druzhinin, "The influence of particle inertia on the two-way coupling and modification of isotropic turbulence by microparticles," *Physics of Fluids,* vol. 13, 2001.
[41] P. Février, O. Simonin, and K. D. Squires, "Partitioning of particle velocities in gas-solid turbulent flows into a continuous field and a spatially uncorrelated random distribution: theoretical formalism and numerical study," *Journal of Fluid Mechanics,* vol. 533, pp. 1-46, 2005.
[42] Y. Xu and S. Subramaniam, "A multiscale model for dilute turbulent gas-particle flows based on the equilibration of energy concept," *Physics of Fluids,* vol. 18, 2006.
[43] M. Abbas, E. Climent, O. Simonin, and M. R. Maxey, "Dynamics of bidisperse suspensions under Stokes flows: Linear shear flow and sedimentation," *Physics of fluids* vol. 18, 2006.
[44] S. V. Apte, M. Martin, and N. A. Patankar, "A numerical method for fully resolved simulation (FRS) of rigid particle-flow interactions in complex flows," *Journal of Computational Physics,* vol. 228, pp. 2712-2738, 2009.
[45] D. R. Greatrix, "Parametric evaluation of solid rocket motor internal ballistics," presented at the 46th AIAA/ASME/SAE/ASEE Joint Propultion Conference & Exhibit, Nashville, TN, 2010.
[46] S. R. Gomes, L. R. Junior, J. A. F. F. Rocco, and K. Iha, "Experimental study of polyurethane-based fuels with addition of paraffin and aluminum for hybrid

rocket motors," *Journal of Aerospace Technology and Management,* vol. 5, pp. 279-286, 2013.
[47] J. Majdalani and A. B. Vyas, "Inviscid models of the classic hybrid rocket," in *AIAA*, 2004-3474, Fort Lauderdale, FL, 2004.
[48] J. Majdalani, "The Taylor-Culick profile with uniform headwall injection," in *AIAA*, 2005-4534, Tucson, AZ, 2005.
[49] A. Davailles, E. Climent, and F. Bourgeois, "Fundamental understanding of swirling flow pattern in hydrocyclones," *Separation and Purification Technology,* vol. 92, pp. 152-160, 2012.
[50] B. Chiné and F. Concha, "Flow patterns in conical and cylindrical hydrocyclones," *Chemical Engineering Journal,* vol. 80, pp. 267-273, 2000.
[51] J. C. Melcher, H. Krier, and R. L. Burton, "Burning aluminum particles inside a laboratory scale solid rocket motor," in *AIAA*, 2001-3947, Salt Lake City, Utah, 2001.
[52] S. V. Alekseenko, P. A. Kuibin, and V. L. Okulov, *Theory of Concentrated Vortices: An Introduction*. Berlin, Germany: Springer, 2007.
[53] O. Lucca-Negro and T. O'Doherty, "Vortex breakdown: A review," *Progress in Energy and Combustion Science,* vol. 27, pp. 431-481, 2001.
[54] J. N. Sørensen, I. V. Namov, and V. L. Okulov, "Multiple helical modes of vortex breakdown," *Journal of Fluid Mechanics,* vol. 683, pp. 430-441, September 2011.
[55] G. Boyer, G. Casalis, and J. L. Estivalèzes, "Stability and sensitivity analysis in a simplified solid rocket motor flow," *Journal of Fluid Mechanics,* vol. 722, pp. 618-644, 2013.
[56] J. Dupays, "Two-phase unsteady flow in solid rocket motors," *Aerospace Science & Technology,* vol. 6, pp. 413-422, 2002.
[57] W. Cai, F. Ma, and V. Yang, "Two-phase vortico-acoustic flow interactions in solid propellant rocket motors," *Journal of Propulsion and Power,* vol. 19, pp. 385-396, 2003.
[58] T. Jackson, F. Najjar, and J. Buckmaster, "New aluminum agglomeration models and their use in solid-propellant-rocket simulations," *Journal of Propulsion and Power,* vol. 21, pp. 925-936, September-October 2005.
[59] V. Morfouace and P. Y. Tissier, "Two-phase flow analysis of instabilities driven by vortex shedding in solid rocket motors," in *AIAA*, 95-2733, San Diego, CA, 1995.
[60] G. Boyer, G. Casalis, and J. L. Estivalèzes, "Stability analysis and numerical simulation of simplified solid rocket motors," *Physics of Fluids,* vol. 25, pp. 084109-084109, 2013.
[61] F. Battaglia, R. G. Rehm, and H. R. Baum, "The fluid mechanics of fire whirls: An inviscid model," *Physics of Fluids,* vol. 12, pp. 2859-2867, 2000.
[62] F. Concha, "Flow pattern in hydrocyclones," *Kona-Powder and Particle,* vol. 25, pp. 97-132, 2007.

[63] G. Avalon, G. Casalis, and J. Griffond, "Flow instabilities and acoustic resonance of channels with wall injection," in *AIAA*, 98-3218, Cleveland, OH, 1998.
[64] S. R. Lin and M. R. Malik, "On the stability of attachment-line boundary layers. Part 1. The incompressible swept Hiemenz flow," *Journal of Fluid Mechanics,* vol. 311, pp. 239-255, 1996.
[65] A. Ogawa, *Vortex Flow*. Boca Raton, Florida: CRC Press, 1993.
[66] G. Arfken, "Mathematical Methods for Physicists," ed Orlando, FL: Academic Press, 1985, pp. 492-493.
[67] M. Abramowitz and I. A. Stegun, *Handbook of Mathematical Functions*. New York: National Bureau of Standards, 1964.
[68] R. L. Burden and J. D. Faires, *Numerical Analysis*, 4 ed.: PWS-KENT Publishing Company, Boston, USA, 1989.
[69] H. Rutishauser, "Solution of eigenvalue problems with the LR transformation," *National Bureau Standards Applied Mathematics Series,* vol. 49, pp. 47-81, 1958.
[70] J. A. Scott, "An Arnoldi Code for Computing Selected Eigenvalues of Sparse, Real, Unsymmetric Matrices," *ACM Transactions on Mathematical Software,* vol. 21, pp. 432-475, 1995.
[71] D. C. Sorensen, "Implicit application of polynomial filters in a k-step Arnoldi method," *SIAM Journal on Matrix Analysis and Applications,* vol. 13, pp. 357-385, 1992.
[72] R. J. Radke, "A Matlab Implementation of the Implicitly Restarted Arnoldi Method for Solving Large-Scale Eigenvalue Problems," Ph.D., Rice University, 1996.
[73] T. Braconnier, V. Fraysse, and J. C. Rioual, "ARNCHEB Users' Guide: Solution of Large Non Symmetric or Non Hermitian Eigenvalue Problems by the Arnoldi-Tchebycheff Method," 1997.
[74] T. S. Elliott, J. W. Batterson, and J. Majdalani, "Biglobal stability of cylindrically-shaped hybrid and solid rockets with injecting or reactive headwalls," in *AIAA*, 2012-3810, Atlanta, GA, 2012.
[75] G. Avalon and D. Lambert, "Cold gas experiments applied to the understanding of aeroacoustic phenomena inside solid propellant boosters," in *AIAA*, 2006-5111, Sacramento, CA, 2006.

Appendix

A.1 Development of Biglobal Equations

Starting with the normalized Navier-Stokes equations the biglobal equations for two-phase flow are derived as follows

The normalized gaseous continuity equation is:

$$\nabla \cdot \tilde{\boldsymbol{U}}_G = 0 \tag{A.1}$$

For cylindrical coordinates this becomes the following:

$$\frac{\partial \tilde{U}_{rG}}{\partial r} + \frac{1}{r}\frac{\partial \tilde{U}_{\theta G}}{\partial \theta} + \frac{\partial \tilde{U}_{zG}}{\partial z} = 0 \tag{A.2}$$

Applying the perturbation:

$$\frac{\partial}{\partial r}\left(U_{rG} + \breve{u}_{rG}\right) + \frac{1}{r}\frac{\partial}{\partial \theta}\left(U_{\theta G} + \breve{u}_{\theta G}\right) + \frac{\partial}{\partial z}\left(U_{zG} + \breve{u}_{zG}\right) = 0 \tag{A.3}$$

Expanding terms and dropping notation for gaseous phase, all components without phase notation will be assumed gaseous:

$$\frac{\partial U_r}{\partial r} + \frac{U_r}{r} + \frac{1}{r}\frac{\partial U_\theta}{\partial \theta} + \frac{\partial U_z}{\partial z} + \frac{\partial \breve{u}_r}{\partial r} + \frac{\breve{u}_r}{r} + \frac{1}{r}\frac{\partial \breve{u}_\theta}{\partial \theta} + \frac{\partial \breve{u}_z}{\partial z} = 0 \tag{A.4}$$

The leading order portion of the equation is known and so all leading order terms are dismissed resulting in:

$$\frac{\partial \breve{u}_r}{\partial r} + \frac{\breve{u}_r}{r} + \frac{1}{r}\frac{\partial \breve{u}_\theta}{\partial \theta} + \frac{\partial \breve{u}_z}{\partial z} = 0 \tag{A.5}$$

The biglobal ansatz is applied resulting in the following:

$$\frac{\partial}{\partial r}\left(u_r \exp\left[i\left(q\theta - \omega t\right)\right]\right) + \frac{1}{r}\left(u_r \exp\left[i\left(q\theta - \omega t\right)\right]\right) + \frac{1}{r}\frac{\partial}{\partial \theta}\left(u_\theta \exp\left[i\left(q\theta - \omega t\right)\right]\right)$$
$$+ \frac{\partial}{\partial z}\left(u_z \exp\left[i\left(q\theta - \omega t\right)\right]\right) = 0 \tag{A.6}$$

$$\exp\left[i\left(q\theta-\omega t\right)\right]\frac{\partial u_r}{\partial r}+u_r\frac{\partial}{\partial r}\left(\exp\left[i\left(q\theta-\omega t\right)\right]\right)+\frac{1}{r}u_r\exp\left[i\left(q\theta-\omega t\right)\right]+\frac{1}{r}\exp\left[i\left(q\theta-\omega t\right)\right]\frac{\partial u_\theta}{\partial \theta}$$
$$+\frac{u_\theta}{r}\frac{\partial}{\partial \theta}\left(\exp\left[i\left(q\theta-\omega t\right)\right]\right)+\exp\left[i\left(q\theta-\omega t\right)\right]\frac{\partial u_z}{\partial z}+u_z\frac{\partial}{\partial z}\left(\exp\left[i\left(q\theta-\omega t\right)\right]\right)=0 \qquad \text{(A.7)}$$

$$\exp\left[i\left(q\theta-\omega t\right)\right]\frac{\partial u_r}{\partial r}+\frac{1}{r}u_r\exp\left[i\left(q\theta-\omega t\right)\right]+\exp\left[i\left(q\theta-\omega t\right)\right]\frac{iqu_\theta}{r}+\exp\left[i\left(q\theta-\omega t\right)\right]\frac{\partial u_z}{\partial z}=0 \qquad \text{(A.8)}$$

Resulting in the final biglobal gaseous continuity equation below.

$$\frac{\partial u_r}{\partial r}+\frac{u_r}{r}+iq\frac{u_\theta}{r}+\frac{\partial u_z}{\partial z}=0 \qquad \text{(A.9)}$$

Moving to the equation of momentum for the gaseous phase, its normalized form is the following:

$$\frac{\partial \tilde{\boldsymbol{U}}_G}{\partial t}+\left(\tilde{\boldsymbol{U}}_G\cdot\nabla\right)\tilde{\boldsymbol{U}}_G=-\nabla\tilde{p}+\frac{1}{Re}\nabla^2\tilde{\boldsymbol{U}}_G-\frac{\tilde{X}_P}{S}\left(\tilde{\boldsymbol{U}}_G-\tilde{\boldsymbol{U}}_P\right) \qquad \text{(A.10)}$$

For cylindrical coordinates, in the radial direction, this becomes the following:

$$\frac{\partial \tilde{U}_{rG}}{\partial t}+\tilde{U}_{rG}\frac{\partial \tilde{U}_{rG}}{\partial r}+\frac{\tilde{U}_{\theta G}}{r}\frac{\partial \tilde{U}_{rG}}{\partial \theta}-\frac{\tilde{U}_{\theta G}^2}{r}+\tilde{U}_{zG}\frac{\partial \tilde{U}_{rG}}{\partial z}+\frac{\partial \tilde{p}}{\partial r}$$
$$=\frac{1}{Re}\left(\frac{\partial^2\tilde{U}_{rG}}{\partial r^2}+\frac{1}{r}\frac{\partial \tilde{U}_{rG}}{\partial r}-\frac{\tilde{U}_{rG}}{r^2}+\frac{1}{r^2}\frac{\partial^2\tilde{U}_{rG}}{\partial \theta^2}-\frac{2}{r^2}\frac{\partial \tilde{U}_{\theta G}}{\partial \theta}+\frac{\partial^2\tilde{U}_{rG}}{\partial z^2}\right)-\frac{\tilde{X}_P}{S}\left(\tilde{U}_{rG}-\tilde{U}_{rP}\right) \qquad \text{(A.11)}$$

Applying the perturbation:

$$\frac{\partial}{\partial t}\left(U_{rG}+\breve{u}_{rG}\right)+\left(U_{rG}+\breve{u}_{rG}\right)\frac{\partial}{\partial r}\left(U_{rG}+\breve{u}_{rG}\right)+\frac{1}{r}\left(U_{\theta G}+\breve{u}_{\theta G}\right)\frac{\partial}{\partial \theta}\left(U_{rG}+\breve{u}_{rG}\right)-\frac{1}{r}\left(U_{\theta G}+\breve{u}_{\theta G}\right)^2$$
$$+\left(U_{zG}+\breve{u}_{zG}\right)\frac{\partial}{\partial z}\left(U_{rG}+\breve{u}_{rG}\right)+\frac{\partial}{\partial r}\left(P+\breve{p}\right)=\frac{1}{Re}\left(\frac{\partial^2}{\partial r^2}\left(U_{rG}+\breve{u}_{rG}\right)+\frac{1}{r}\frac{\partial}{\partial r}\left(U_{rG}+\breve{u}_{rG}\right)-\frac{1}{r^2}\left(U_{rG}+\breve{u}_{rG}\right)\right.$$
$$\left.+\frac{1}{r^2}\frac{\partial^2}{\partial \theta^2}\left(U_{rG}+\breve{u}_{rG}\right)-\frac{2}{r^2}\frac{\partial}{\partial \theta}\left(U_{\theta G}+\breve{u}_{\theta G}\right)+\frac{\partial^2}{\partial z^2}\left(U_{rG}+\breve{u}_{rG}\right)\right)$$
$$-\frac{\left(X_P+\breve{x}_P\right)}{S}\left(\left(U_{rG}+\breve{u}_{rG}\right)-\left(U_{rP}+\breve{u}_{rP}\right)\right) \qquad \text{(A.12)}$$

Expanding terms and dropping notation for gaseous phase, all components without phase notation will be assumed gaseous:

$$
\begin{aligned}
&\frac{\partial U_{rG}}{\partial t}+\frac{\partial \breve{u}_{rG}}{\partial t}+U_{rG}\frac{\partial U_{rG}}{\partial r}+U_{rG}\frac{\partial \breve{u}_{rG}}{\partial r}+\breve{u}_{rG}\frac{\partial U_{rG}}{\partial r}+\breve{u}_{rG}\frac{\partial \breve{u}_{rG}}{\partial r}+\frac{1}{r}\left(U_{\theta G}\frac{\partial U_{rG}}{\partial \theta}+U_{\theta G}\frac{\partial \breve{u}_{rG}}{\partial \theta}+\breve{u}_{\theta G}\frac{\partial U_{rG}}{\partial \theta}\right.\\
&\quad\left.+\breve{u}_{\theta G}\frac{\partial \breve{u}_{rG}}{\partial \theta}\right)-\frac{1}{r}\left(2\breve{u}_{\theta G}U_{\theta G}+\breve{u}_{\theta G}^{2}+U^{2}{}_{\theta G}\right)+U_{zG}\frac{\partial U_{rG}}{\partial z}+U_{zG}\frac{\partial \breve{u}_{rG}}{\partial z}+\breve{u}_{zG}\frac{\partial U_{rG}}{\partial z}+\breve{u}_{zG}\frac{\partial \breve{u}_{rG}}{\partial z}+\frac{\partial p}{\partial r}\\
&\quad+\frac{\partial \breve{p}}{\partial r}=\frac{1}{Re}\left(\frac{\partial^2 U_{rG}}{\partial r^2}+\frac{\partial^2 \breve{u}_{rG}}{\partial r^2}+\frac{1}{r}\frac{\partial U_{rG}}{\partial r}+\frac{1}{r}\frac{\partial \breve{u}_{rG}}{\partial r}-\frac{1}{r^2}\left(U_{rG}+\breve{u}_{rG}\right)+\frac{1}{r^2}\frac{\partial^2 U_{rG}}{\partial \theta^2}+\frac{1}{r^2}\frac{\partial^2 \breve{u}_{rG}}{\partial \theta^2}\right.\\
&\quad\left.-\frac{2}{r^2}\frac{\partial U_{\theta G}}{\partial \theta}-\frac{2}{r^2}\frac{\partial \breve{u}_{\theta G}}{\partial \theta}+\frac{\partial^2 U_{rG}}{\partial z^2}+\frac{\partial^2 \breve{u}_{rG}}{\partial z^2}\right)-\frac{\left(X_P+\breve{x}_P\right)}{S}\left(\left(U_{rG}+\breve{u}_{rG}\right)-\left(U_{rP}+\breve{u}_{rP}\right)\right)
\end{aligned}
\tag{A.13}
$$

Grouping similar terms we find

$$
\begin{aligned}
&\frac{\partial U_r}{\partial t}+U_r\frac{\partial U_r}{\partial r}+\frac{U_\theta}{r}\frac{\partial U_r}{\partial \theta}-\frac{U_\theta^2}{r}+U_z\frac{\partial U_r}{\partial z}+\frac{\partial p}{\partial r}\\
&\quad+\frac{\partial \breve{u}_r}{\partial t}+U_r\frac{\partial \breve{u}_r}{\partial r}+\breve{u}_r\frac{\partial U_r}{\partial r}+\frac{U_\theta}{r}\frac{\partial \breve{u}_r}{\partial \theta}+\frac{\breve{u}_\theta}{r}\frac{\partial U_r}{\partial \theta}-\frac{2U_\theta \breve{u}_\theta}{r}+U_z\frac{\partial \breve{u}_r}{\partial z}+\breve{u}_z\frac{\partial U_r}{\partial z}+\frac{\partial \breve{p}}{\partial r}\\
&\quad+\breve{u}_r\frac{\partial \breve{u}_r}{\partial r}+\frac{\breve{u}_\theta}{r}\frac{\partial \breve{u}_r}{\partial \theta}-\frac{\breve{u}_\theta^2}{r}+\breve{u}_z\frac{\partial \breve{u}_r}{\partial z}\\
&=\frac{1}{Re}\left(\frac{\partial^2 U_r}{\partial r^2}+\frac{1}{r}\frac{\partial U_r}{\partial r}-\frac{U_r}{r^2}+\frac{1}{r^2}\frac{\partial^2 U_r}{\partial \theta^2}-\frac{2}{r^2}\frac{\partial U_\theta}{\partial \theta}+\frac{\partial^2 U_r}{\partial z^2}+\frac{\partial^2 \breve{u}_r}{\partial r^2}+\frac{1}{r}\frac{\partial \breve{u}_r}{\partial r}-\frac{\breve{u}_r}{r^2}+\frac{1}{r^2}\frac{\partial^2 \breve{u}_r}{\partial \theta^2}-\frac{2}{r^2}\frac{\partial \breve{u}_\theta}{\partial \theta}+\frac{\partial^2 \breve{u}_r}{\partial z^2}\right)\\
&\quad-\frac{X_P}{S}\left(U_r-U_{rP}+\breve{u}_r-\breve{u}_{rP}\right)-\frac{\breve{x}_P}{S}\left(U_r-U_{rP}\right)-\frac{\breve{x}_P}{S}\left(\breve{u}_r-\breve{u}_{rP}\right)
\end{aligned}
\tag{A.14}
$$

The leading order terms are known and are dismissed. Our concern is the first order solution so second order terms are neglected resulting in:

$$
\begin{aligned}
&\frac{\partial \breve{u}_r}{\partial t}+U_r\frac{\partial \breve{u}_r}{\partial r}+\breve{u}_r\frac{\partial U_r}{\partial r}+\frac{U_\theta}{r}\frac{\partial \breve{u}_r}{\partial \theta}+\frac{\breve{u}_\theta}{r}\frac{\partial U_r}{\partial \theta}-\frac{2U_\theta \breve{u}_\theta}{r}+U_z\frac{\partial \breve{u}_r}{\partial z}+\breve{u}_z\frac{\partial U_r}{\partial z}+\frac{\partial \breve{p}}{\partial r}\\
&\quad=\varepsilon\left(\frac{\partial^2 \breve{u}_r}{\partial r^2}+\frac{1}{r}\frac{\partial \breve{u}_r}{\partial r}-\frac{\breve{u}_r}{r^2}+\frac{1}{r^2}\frac{\partial^2 \breve{u}_r}{\partial \theta^2}-\frac{2}{r^2}\frac{\partial \breve{u}_\theta}{\partial \theta}+\frac{\partial^2 \breve{u}_r}{\partial z^2}\right)\\
&\quad-\frac{X_P}{S}\left(\breve{u}_r-\breve{u}_{rP}\right)-\frac{\breve{x}_P}{S}\left(U_r-U_{rP}\right)
\end{aligned}
\tag{A.15}
$$

The biglobal ansatz is applied resulting in the following:

$$
\begin{aligned}
&\frac{\partial}{\partial t}\left(u_r \exp\left[i\left(q\theta-\omega t\right)\right]\right)+U_r\frac{\partial}{\partial r}\left(u_r \exp\left[i\left(q\theta-\omega t\right)\right]\right)+\left(u_r \exp\left[i\left(q\theta-\omega t\right)\right]\right)\frac{\partial U_r}{\partial r}\\
&\quad+\frac{U_\theta}{r}\frac{\partial}{\partial\theta}\left(u_r \exp\left[i\left(q\theta-\omega t\right)\right]\right)+\frac{1}{r}\left(u_\theta \exp\left[i\left(q\theta-\omega t\right)\right]\right)\frac{\partial U_r}{\partial\theta}-\frac{2U_\theta}{r}\left(u_\theta \exp\left[i\left(q\theta-\omega t\right)\right]\right)\\
&\quad+U_z\frac{\partial}{\partial z}\left(u_r \exp\left[i\left(q\theta-\omega t\right)\right]\right)+\left(u_z \exp\left[i\left(q\theta-\omega t\right)\right]\right)\frac{\partial U_r}{\partial z}+\frac{\partial}{\partial r}\left(p \exp\left[i\left(q\theta-\omega t\right)\right]\right)\\
&\quad=\varepsilon\left(\frac{\partial^2}{\partial r^2}\left(u_r \exp\left[i\left(q\theta-\omega t\right)\right]\right)+\frac{1}{r}\frac{\partial}{\partial r}\left(u_r \exp\left[i\left(q\theta-\omega t\right)\right]\right)-\frac{1}{r^2}\left(u_r \exp\left[i\left(q\theta-\omega t\right)\right]\right)\right.\\
&\quad\left.+\frac{1}{r^2}\frac{\partial^2}{\partial\theta^2}\left(u_r \exp\left[i\left(q\theta-\omega t\right)\right]\right)-\frac{2}{r^2}\frac{\partial}{\partial\theta}\left(u_\theta \exp\left[i\left(q\theta-\omega t\right)\right]\right)+\frac{\partial^2}{\partial z^2}\left(u_r \exp\left[i\left(q\theta-\omega t\right)\right]\right)\right)\\
&\quad-\frac{X_P}{S}\left(\left(u_r \exp\left[i\left(q\theta-\omega t\right)\right]\right)-\left(u_{rP} \exp\left[i\left(q\theta-\omega t\right)\right]\right)\right)\\
&\quad-\frac{\left(x_P \exp\left[i\left(q\theta-\omega t\right)\right]\right)}{S}\left(U_r-U_{rP}\right)
\end{aligned}
\tag{A.16}
$$

After differentiation and division by the common exponential term the resulting equation is the final biglobal gaseous radial momentum equation below.

$$
\begin{aligned}
&-i\omega u_r+U_r\frac{\partial u_r}{\partial r}+u_r\frac{\partial U_r}{\partial r}+\frac{U_\theta qi}{r}u_r+\frac{u_\theta}{r}\frac{\partial U_r}{\partial\theta}-\frac{2U_\theta u_\theta}{r}+U_z\frac{\partial u_r}{\partial z}+u_z\frac{\partial U_r}{\partial z}+\frac{\partial p}{\partial r}\\
&\quad=\varepsilon\left(\frac{\partial^2 u_r}{\partial r^2}+\frac{1}{r}\frac{\partial u_r}{\partial r}-\frac{u_r}{r^2}-\frac{q^2}{r^2}u_r-\frac{2iq}{r^2}u_\theta+\frac{\partial^2 u_r}{\partial z^2}\right)\\
&\quad-\frac{X_P}{S}\left(u_r-u_{rP}\right)-\frac{x_P}{S}\left(U_r-U_{rP}\right)
\end{aligned}
\tag{A.17}
$$

Following the same procedure the final biglobal gaseous tangential and axial momentum equations are

$$
\begin{aligned}
&-i\omega u_\theta+U_r\frac{\partial u_\theta}{\partial r}+u_r\frac{\partial U_\theta}{\partial r}+\frac{iqU_\theta}{r}u_\theta+\frac{u_\theta}{r}\frac{\partial U_\theta}{\partial\theta}+\frac{U_\theta u_r}{r}+\frac{U_r u_\theta}{r}+U_z\frac{\partial u_\theta}{\partial z}+u_z\frac{\partial U_\theta}{\partial z}+\frac{iq}{r}p\\
&\quad=\varepsilon\left(\frac{\partial^2 u_\theta}{\partial r^2}+\frac{1}{r}\frac{\partial u_\theta}{\partial r}-\frac{u_\theta}{r^2}-\frac{q^2}{r^2}u_\theta+\frac{2iq}{r^2}u_r+\frac{\partial^2 u_\theta}{\partial z^2}\right)\\
&\quad-\frac{X_P}{S}\left(u_\theta-u_{\theta P}\right)-\frac{x_P}{S}\left(U_\theta-U_{\theta P}\right)
\end{aligned}
\tag{A.18}
$$

$$-i\omega u_z + U_r \frac{\partial u_z}{\partial r} + u_r \frac{\partial U_z}{\partial r} + \frac{iqU_\theta}{r} u_z + \frac{u_\theta}{r}\frac{\partial U_z}{\partial \theta} + U_z \frac{\partial u_z}{\partial z} + u_z \frac{\partial U_z}{\partial z} + \frac{\partial p}{\partial z} = \varepsilon\left(\frac{\partial^2 u_z}{\partial r^2} + \frac{1}{r}\frac{\partial u_z}{\partial r} - \frac{q^2}{r^2}u_z + \frac{\partial^2 u_z}{\partial z^2}\right) - \frac{X_P}{S}\left(u_z - u_{zP}\right) - \frac{x_P}{S}\left(U_z - U_{zP}\right) \tag{A.19}$$

Turning attention to the particle phase the normalized particle continuity equation is:

$$\frac{\partial \tilde{X}_P}{\partial t} + \nabla\cdot\left(\tilde{X}_P \tilde{\boldsymbol{U}}_P\right) = 0 \tag{A.20}$$

For cylindrical coordinates this becomes the following:

$$\frac{\partial \tilde{X}_P}{\partial t} + \frac{1}{r}\frac{\partial r\tilde{X}_P\tilde{U}_{rP}}{\partial r} + \frac{1}{r}\frac{\partial \tilde{X}_P\tilde{U}_{\theta P}}{\partial \theta} + \frac{\partial \tilde{X}_P\tilde{U}_{zP}}{\partial z} \tag{A.21}$$

Applying the perturbation:

$$\frac{\partial}{\partial t}\left(X_P + \breve{x}_P\right) + \frac{1}{r}\frac{\partial}{\partial r}\left[r\left(X_P + \breve{x}_P\right)\left(U_{rP} + \breve{u}_{rP}\right)\right] + \frac{1}{r}\frac{\partial}{\partial \theta}\left[\left(X_P + \breve{x}_P\right)\left(U_{\theta P} + \breve{u}_{\theta P}\right)\right] + \frac{\partial}{\partial z}\left[\left(X_P + \breve{x}_P\right)\left(U_{zP} + \breve{u}_{zP}\right)\right] \tag{A.22}$$

Expanding terms:

$$\frac{\partial X_P}{\partial t} + \frac{\partial \breve{x}_P}{\partial t} + \frac{1}{r}\frac{\partial}{\partial r}\left(rX_PU_{rP} + rX_P\breve{u}_{rP} + rU_{rP}\breve{x}_P + r\breve{x}_P\breve{u}_{rP}\right) + \frac{1}{r}\frac{\partial}{\partial \theta}\left(X_PU_{\theta P} + X_P\breve{u}_{\theta P} + U_{\theta P}\breve{x}_P + \breve{x}_P\breve{u}_{\theta P}\right) + \frac{\partial}{\partial z}\left(X_PU_{zP} + X_P\breve{u}_{zP} + U_{zP}\breve{x}_P + \breve{x}_P\breve{u}_{zP}\right) \tag{A.23}$$

Grouping similar terms:

$$\frac{\partial X_P}{\partial t} + \frac{1}{r}\frac{\partial rX_PU_{rP}}{\partial r} + \frac{1}{r}\frac{\partial X_PU_{\theta P}}{\partial \theta} + \frac{\partial X_PU_{zP}}{\partial z} + \frac{\partial \breve{x}_P}{\partial t} + \frac{1}{r}\frac{\partial rU_{rP}\breve{x}_P}{\partial r} + \frac{1}{r}\frac{\partial rX_P\breve{u}_{rP}}{\partial r} + \frac{1}{r}\frac{\partial U_{\theta P}\breve{x}_P}{\partial \theta} + \frac{1}{r}\frac{\partial X_P\breve{u}_{\theta P}}{\partial \theta} + \frac{\partial U_{zP}\breve{x}_P}{\partial z} + \frac{\partial X_P\breve{u}_{zP}}{\partial z} + \frac{1}{r}\frac{\partial r\breve{x}_P\breve{u}_{rP}}{\partial r} + \frac{1}{r}\frac{\partial \breve{x}_P\breve{u}_{\theta P}}{\partial \theta} + \frac{\partial \breve{x}_P\breve{u}_{zP}}{\partial z} = 0 \tag{A.24}$$

The leading order terms are known and are dismissed. Our concern is the first order solution so second order terms are neglected resulting in:

$$\frac{\partial \breve{x}_P}{\partial t}+\frac{1}{r}\frac{\partial rU_{rP}\breve{x}_P}{\partial r}+\frac{1}{r}\frac{\partial rX_P\breve{u}_{rP}}{\partial r}+\frac{1}{r}\frac{\partial U_{\theta P}\breve{x}_P}{\partial \theta}+\frac{1}{r}\frac{\partial X_P\breve{u}_{\theta P}}{\partial \theta}+\frac{\partial U_{zP}\breve{x}_P}{\partial z}+\frac{\partial X_P\breve{u}_{zP}}{\partial z}=0 \tag{A.25}$$

The biglobal ansatz is applied resulting in the following:

$$\begin{aligned}\frac{\partial}{\partial t}\left(x_P \exp\left[i\left(q\theta-\omega t\right)\right]\right)+\frac{1}{r}\frac{\partial}{\partial r}\left(rU_{rP}x_P \exp\left[i\left(q\theta-\omega t\right)\right]\right)+\frac{1}{r}\frac{\partial}{\partial r}\left(rX_Pu_{rP} \exp\left[i\left(q\theta-\omega t\right)\right]\right)\\+\frac{1}{r}\frac{\partial}{\partial \theta}\left(U_{\theta P}x_P \exp\left[i\left(q\theta-\omega t\right)\right]\right)+\frac{1}{r}\frac{\partial}{\partial \theta}\left(X_Pu_{\theta P} \exp\left[i\left(q\theta-\omega t\right)\right]\right)\\+\frac{\partial}{\partial z}\left(U_{zP}x_P \exp\left[i\left(q\theta-\omega t\right)\right]\right)+\frac{\partial}{\partial z}\left(X_Pu_{zP} \exp\left[i\left(q\theta-\omega t\right)\right]\right)=0\end{aligned} \tag{A.26}$$

After differentiation and division by the common exponential term the resulting equation is the final biglobal particle continuity equation below.

$$\begin{aligned}-i\omega x_P+\frac{1}{r}\left[U_{rP}x_P+X_Pu_{rP}+x_P\frac{\partial U_{\theta P}}{\partial \theta}+U_{\theta P}iqx_P+X_Piqu_{\theta P}+u_{\theta P}\frac{\partial X_P}{\partial \theta}\right]+x_P\frac{\partial U_{rP}}{\partial r}+U_{rP}\frac{\partial x_P}{\partial r}\\+u_{rP}\frac{\partial X_P}{\partial r}+X_P\frac{\partial u_{rP}}{\partial r}+x_P\frac{\partial U_{zP}}{\partial z}+U_{zP}\frac{\partial x_P}{\partial z}+X_P\frac{\partial u_{zP}}{\partial z}+u_{zP}\frac{\partial X_P}{\partial z}=0\end{aligned} \tag{A.27}$$

Moving to the equation of momentum for the particle phase, its normalized form is the following:

$$\frac{\partial \tilde{\boldsymbol{U}}_P}{\partial t}+\left(\tilde{\boldsymbol{U}}_P\cdot\nabla\right)\tilde{\boldsymbol{U}}_P=\frac{1}{S}\left(\tilde{\boldsymbol{U}}_G-\tilde{\boldsymbol{U}}_P\right) \tag{A.28}$$

For cylindrical coordinates, in the radial direction, this becomes the following:

$$\frac{\partial \tilde{U}_{rP}}{\partial t}+\tilde{U}_{rP}\frac{\partial \tilde{U}_{rP}}{\partial r}+\frac{\tilde{U}_{\theta P}}{r}\frac{\partial \tilde{U}_{rP}}{\partial \theta}+\tilde{U}_{zP}\frac{\partial \tilde{U}_{rP}}{\partial z}=\frac{1}{S}\left(\tilde{U}_r-\tilde{U}_{rP}\right) \tag{A.29}$$

Applying the perturbation:

$$\frac{\partial}{\partial t}\left(U_{rP}+\breve{u}_{rP}\right)+\left(U_{rP}+\breve{u}_{rP}\right)\frac{\partial}{\partial r}\left(U_{rP}+\breve{u}_{rP}\right)+\left(U_{\theta P}+\breve{u}_{\theta P}\right)\frac{1}{r}\frac{\partial}{\partial \theta}\left(U_{rP}+\breve{u}_{rP}\right)$$
$$+\left(U_{zP}+\breve{u}_{zP}\right)\frac{\partial}{\partial z}\left(U_{rP}+\breve{u}_{rP}\right)=\frac{1}{S}\left(\left(U_{r}+\breve{u}_{r}\right)-\left(U_{rP}+\breve{u}_{rP}\right)\right) \tag{A.30}$$

Expanding and grouping terms:

$$\frac{\partial U_{rP}}{\partial t}+U_{rP}\frac{\partial U_{rP}}{\partial r}+\frac{U_{\theta P}}{r}\frac{\partial U_{rP}}{\partial \theta}+U_{zP}\frac{\partial U_{rP}}{\partial z}$$
$$+\frac{\partial \breve{u}_{rP}}{\partial t}+U_{rP}\frac{\partial \breve{u}_{rP}}{\partial r}+\breve{u}_{rP}\frac{\partial U_{rP}}{\partial r}+\frac{U_{\theta P}}{r}\frac{\partial \breve{u}_{rP}}{\partial \theta}+\frac{\breve{u}_{\theta P}}{r}\frac{\partial U_{rP}}{\partial \theta}+U_{zP}\frac{\partial \breve{u}_{rP}}{\partial z}+\breve{u}_{zP}\frac{\partial U_{rP}}{\partial z}$$
$$+\breve{u}_{rP}\frac{\partial \breve{u}_{rP}}{\partial r}+\frac{\breve{u}_{\theta P}}{r}\frac{\partial \breve{u}_{rP}}{\partial \theta}+\breve{u}_{zP}\frac{\partial \breve{u}_{rP}}{\partial z}$$
$$=\frac{1}{S}\left(U_{r}-U_{rP}+\breve{u}_{r}-\breve{u}_{rP}\right) \tag{A.31}$$

The leading order terms are known and are dismissed. Our concern is the first order solution so second order terms are neglected resulting in:

$$\frac{\partial \breve{u}_{rP}}{\partial t}+U_{rP}\frac{\partial \breve{u}_{rP}}{\partial r}+\breve{u}_{rP}\frac{\partial U_{rP}}{\partial r}+\frac{U_{\theta P}}{r}\frac{\partial \breve{u}_{rP}}{\partial \theta}+\frac{\breve{u}_{\theta P}}{r}\frac{\partial U_{rP}}{\partial \theta}+U_{zP}\frac{\partial \breve{u}_{rP}}{\partial z}+\breve{u}_{zP}\frac{\partial U_{rP}}{\partial z}=\frac{1}{S}\left(\breve{u}_{r}-\breve{u}_{rP}\right) \tag{A.32}$$

The biglobal ansatz is applied resulting in the following:

$$\frac{\partial}{\partial t}u_{rP}\exp\left[i\left(q\theta-\omega t\right)\right]+U_{rP}\frac{\partial}{\partial r}u_{rP}\exp\left[i\left(q\theta-\omega t\right)\right]+u_{rP}\exp\left[i\left(q\theta-\omega t\right)\right]\frac{\partial U_{rP}}{\partial r}$$
$$+\frac{U_{\theta P}}{r}\frac{\partial}{\partial \theta}u_{rP}\exp\left[i\left(q\theta-\omega t\right)\right]+\frac{1}{r}u_{\theta P}\exp\left[i\left(q\theta-\omega t\right)\right]\frac{\partial U_{rP}}{\partial \theta}+U_{zP}\frac{\partial}{\partial z}u_{rP}\exp\left[i\left(q\theta-\omega t\right)\right]$$
$$+u_{zP}\exp\left[i\left(q\theta-\omega t\right)\right]\frac{\partial U_{rP}}{\partial z}=\frac{1}{S}\left(u_{r}\exp\left[i\left(q\theta-\omega t\right)\right]-u_{rP}\exp\left[i\left(q\theta-\omega t\right)\right]\right) \tag{A.33}$$

After differentiation and division by the common exponential term the resulting equation is the final biglobal particle radial momentum equation below.

$$-i\omega u_{rP}+U_{rP}\frac{\partial u_{rP}}{\partial r}+u_{rP}\frac{\partial U_{rP}}{\partial r}+\frac{U_{\theta P}}{r}iqu_{rP}+\frac{u_{\theta P}}{r}\frac{\partial U_{rP}}{\partial \theta}+U_{zP}\frac{\partial u_{rP}}{\partial z}+u_{zP}\frac{\partial U_{rP}}{\partial z}=\frac{1}{S}\left(u_{r}-u_{rP}\right) \tag{A.34}$$

Following the same procedure the final biglobal particle tangential and axial momentum equations are

$$-i\omega u_{\theta P}+U_{rP}\frac{\partial u_{\theta P}}{\partial r}+u_{rP}\frac{\partial U_{\theta P}}{\partial r}+\frac{U_{\theta P}}{r}iqu_{\theta P}+\frac{u_{\theta P}}{r}\frac{\partial U_{\theta P}}{\partial \theta}+U_{zP}\frac{\partial u_{\theta P}}{\partial z}+u_{zP}\frac{\partial U_{\theta P}}{\partial z}=\frac{1}{S}\left(u_{\theta}-u_{\theta P}\right) \quad \text{(A.35)}$$

$$-i\omega u_{zP}+U_{rP}\frac{\partial u_{zP}}{\partial r}+u_{rP}\frac{\partial U_{zP}}{\partial r}+\frac{U_{\theta P}}{r}iqu_{zP}+\frac{u_{\theta P}}{r}\frac{\partial U_{zP}}{\partial \theta}+U_{zP}\frac{\partial u_{zP}}{\partial z}+u_{zP}\frac{\partial U_{zP}}{\partial z}=\frac{1}{S}\left(u_{z}-u_{zP}\right) \quad \text{(A.36)}$$

Vita

Trevor Sterling Elliott was born in Orlando, Florida on September 11, 1981 to Robert H. and Janet S. Elliott. He attended The University of Tennessee at Chattanooga where he graduated in the summer of 2005, earning a Bachelor of Engineering degree in Mechanical Engineering. In 2006 he started a Master of Science in Mechanical Engineering. This degree was completed in the winter of 2009 with a thesis on Internal Engine Combustion analysis and the creation of a laboratory apparatus for undergraduate education. Before the completion of his Master's thesis Trevor enrolled in the Ph.D. program in fall of 2008. In this same period he achieved his greatest accomplishment to date, marrying his true love Ulyana V. Pugina. Through the guidance and mentorship of his major Professor Joseph Majdalani, he found his home in an Aerospace specialization. During his Masters and Ph.D. course work he worked fulltime at the University of Tennessee at Chattanooga. In the research and dissertation stage he maintained the same fulltime job and served as an adjunct instructor teaching fluid mechanics laboratories and the senior engineering design sequence at UTC. For his Ph.D., Trevor improved upon a framework for the stability of rocket engines.